

Cretaceous oblique extensional deformation and magma accumulation in the Fosdick Mountains migmatite-cored gneiss dome, West Antarctica

R. R. McFadden,^{1,2} C. S. Siddoway,³ C. Teyssier,¹ and C. M. Fanning⁴

Received 19 March 2009; revised 12 March 2010; accepted 25 March 2010; published 6 August 2010.

[1] The Fosdick Mountains, West Antarctica, expose a 15 x 80 km migmatite-cored gneiss dome consisting of migmatitic gneisses, diatexite migmatite, and subhorizontal leucogranite sheets. The Fosdick dome was emplaced and exhumed in the mid-Cretaceous due to oblique extension associated with the West Antarctic Rift system along the West Antarctic–New Zealand segment of East Gondwana. The dome is bounded to the south by a dextral oblique detachment structure and to the north by an inferred dextral strike-slip fault. Within the Fosdick dome and in the detachment zone, granite occupies leucosomes, dikes, sills, and dilatant and shear structures. The pattern of kilometer-scale domains of migmatite and granite suggest that lithologic variations and heterogeneous deformation (boudinage) resulted in pressure gradients that enhanced melt flow and magma accumulation in the Fosdick dome. Steep foliations are overprinted, folded, and transposed by subhorizontal fabrics. The crosscutting relationship is interpreted as a transition from wrench deformation to oblique divergence. Steep structures in the dome host concordant, subvertical leucosome and granite sheets yielding SHRIMP U–Pb zircon ages between ca. 117 and 114 Ma. Prevalent subhorizontal domains host large volumes of subhorizontal diatexite migmatite and granite sheets that yield U–Pb zircon ages between ca. 109 and 102 Ma. These ages indicate a timescale for melt influx of approximately 15 Ma and that the transition from wrench to oblique divergence may have occurred in as little as 5 Ma. Granites with crystallization ages between ca. 109 and 102 Ma were also emplaced in the South Fosdick Detachment zone, indicating that the detachment was active during oblique divergence. SHRIMP U–Pb titanite ages between ca. 102 and 97 Ma for late- to post-tectonic diorite dikes are interpreted as

emplacement ages and give a minimum age for gneissic foliation development during detachment faulting. The Fosdick Mountains preserve a record of the middle to lower crustal response to a transition from wrench to oblique extensional deformation. Overprinting structural relationships show that a change in the angle of oblique extension can induce accumulation of subhorizontal magma sheets and lead to initiation of a detachment zone. **Citation:** McFadden, R. R., C. S. Siddoway, C. Teyssier, and C. M. Fanning (2010), Cretaceous oblique extensional deformation and magma accumulation in the Fosdick Mountains migmatite-cored gneiss dome, West Antarctica, *Tectonics*, 29, TC4022, doi:10.1029/2009TC002492.

1. Introduction

[2] Structural and petrological investigations of migmatite terrains have refined our view of the fundamental role crustal melting plays in advection of heat and mass and the mechanical evolution of collisional and accretionary orogens [Vernon *et al.*, 1990; Sawyer, 1996, 2001; Brown, 1994; Brown and Solar, 1998b; Milord *et al.*, 2001; Vanderhaeghe, 2001; Teyssier and Whitney, 2002; Marchildon and Brown, 2003; Olsen *et al.*, 2004; Teyssier *et al.*, 2005; Bellot, 2007; Brown, 2007; Hasalová *et al.*, 2008]. Exhumed migmatite-cored gneiss domes represent domains of crystallized formerly partially molten crust that offer direct access to the km-scale structural architecture of melt-dominated middle and lower crust where the relationship between melt migration and deformation processes can be studied [e.g., Collins and Sawyer, 1996; Sawyer, 2001; Solar and Brown, 2001; Weinberg and Mark, 2008]. These relationships are fundamental because melt transfer affects the thermal structure of the crust, and the km-scale distribution of migmatite and granite units may influence the behavior of rheologically layered crust. The previous studies raise an important question about melt distribution and melt transfer in orogenic crust: What are the controls exerted by the anisotropy that arises from lithologic heterogeneities and by tectonic structures (e.g., detachment zones, strike-slip faults) on the distribution of discrete melt or magma bodies?

[3] In order to address this question, access to regional-scale systems is needed, where the spatial and temporal relationships between the distribution of melt in a migmatite terrain and large tectonic structures can be determined. The regional perspective is essential to crustal flow and crustal differentiation studies [e.g., Brown and Solar, 1998a; Solar and Brown, 2001; Weinberg *et al.*, 2009], however mig-

¹Department of Geology and Geophysics, University of Minnesota, Minneapolis, Minnesota, USA.

²Now at Smithsonian Tropical Research Institute, Ancon, Panama.

³Department of Geology, Colorado College, Colorado Springs, Colorado, USA.

⁴Research School Earth Sciences, Australian National University, Canberra, ACT, Australia.

matite investigations commonly focus on the outcrop-scale [e.g., *Marchildon and Brown*, 2003] because natural exposures are not extensive due to cover and limited relief. The Fosdick Mountains of West Antarctica offer extensive lateral and vertical exposures of migmatite and granite within a gneiss dome that formed during regional oblique rifting associated with middle Cretaceous opening of the West Antarctic Rift system [*Siddoway et al.*, 2004b; *Siddoway*, 2008].

[4] In wrench and transtensional settings, understanding the three-dimensional configuration of fabrics is crucial for the study of the evolution of strain and magma migration in the crust [e.g., *Brown and Solar*, 1998a; *Solar and Brown*, 2001; *McFadden et al.*, 2010]. Dilation zones may develop due to deformation as well as lithologic heterogeneities that exist along large strike-slip faults, creating pressure gradients for ascent and emplacement of magma and partially molten crust [e.g., *Hutton*, 1988; *D'Lemos et al.*, 1992; *Tikoff and Teyssier*, 1992; *Talbot et al.*, 2005; *Weinberg et al.*, 2009]. Migmatite-cored gneiss domes and core complexes may be emplaced in dilation zones [*Oldow*, 2003; *Talbot et al.*, 2005; *Foster et al.*, 2007; *Whitney et al.*, 2007] that focus melt transport, magma accumulation, and formation of detachments [e.g., *Brown and Solar*, 1998a; *Teyssier et al.*, 2005; *Weinberg and Mark*, 2008; *Weinberg et al.*, 2009].

[5] According to transtension theory, the divergence angle, α , between the motion vector and the established boundary faults, controls the strain field and the fabrics that develop. For $0^\circ < \alpha < 20^\circ$, wrench-dominated transtension occurs and for $20^\circ < \alpha < 90^\circ$, extension-dominated transtension develops [*Fossen and Tikoff*, 1993; *Tikoff and Teyssier*, 1994]. Vertical foliation and horizontal lineation prevail during wrench deformation, but in wrench-dominated transtension, the material undergoes constriction to produce an L-tectonite, and with increasing strain, foliation switches to horizontal as it strengthens again. If the divergence angle is $>20^\circ$, foliation forms and remains horizontal whatever the amount of strain [*Fossen and Tikoff*, 1993; *Teyssier and Tikoff*, 1999].

[6] In an effort to explore the relationships between oblique extensional deformation, magma migration, and magma emplacement, this study examines an ~8 km-thick section of crust exposed within the Fosdick Mountains migmatite-cored gneiss dome in western Marie Byrd Land (Figures 1 and 2). We describe field observations, document the km-scale architecture, and present results of SHRIMP U-Pb zircon and titanite geochronology that document the kinematic and temporal evolution during a change from wrenching to oblique extension that led to emplacement of the dome. We show that early steep foliations that transferred melt efficiently were overprinted by subhorizontal foliations that led to ponding of granitic magma, initiation of detachment tectonics, exhumation, and crystallization of the migmatite-cored gneiss dome.

2. Regional Geologic Setting

[7] The Fosdick Mountains are situated in the Ford Ranges on the eastern margin of the Ross Sea, bordering the

Southern Ocean (Figure 1a). Formation of the vast West Antarctic Rift system in Cretaceous time thinned the Marie Byrd Land crust where the Ford Ranges are found [*Storey et al.*, 1999; *Luyendyk et al.*, 2003; *Siddoway et al.*, 2004a, 2005; *Siddoway*, 2008]. Cretaceous extension affected the wide accretionary zone developed in Paleozoic-Mesozoic time along the East Gondwana margin, which corresponds to present-day West Antarctica and Zealandia (New Zealand + submarine plateaux) [*Luyendyk*, 1995; *Mortimer et al.*, 2006] (Figure 1b). Extension occurred inboard of the Mesozoic magmatic arc that was constructed upon then contiguous West Antarctica–Zealandia [*Bradshaw et al.*, 1997; *Mortimer et al.*, 1999] and led to the formation of the core complexes of South Island, New Zealand [*Tulloch and Kimbrough*, 1989; *Forster and Lister*, 2003], deep level shear zones in Fiordland [*Gibson et al.*, 1988; *Scott and Cooper*, 2006], oblique detachment structures in the Fosdick Mountains, West Antarctica [*McFadden et al.*, 2007], and detachment structures in the Ross Sea [*Fitzgerald and Baldwin*, 1997; *Siddoway et al.*, 2004a] (Figure 1).

[8] U-Pb ages document the timeframe of crustal thinning and concomitant crustal heating of the Gondwana margin [*Davey and Brancolini*, 1995; *Tulloch et al.*, 2006; *Siddoway*, 2008]. U-Pb ages on accessory minerals within gneisses affected by high temperature metamorphism and anatexis in Fiordland, New Zealand, are ca. 126–110 Ma [*Hollis et al.*, 2004; *Ireland and Gibson*, 1998; *Flowers et al.*, 2005; *Scott and Cooper*, 2006] and in the Paparoa metamorphic core complex, New Zealand, are ca. 119–109 Ma [*Kimbrough and Tulloch*, 1989; *Ireland and Gibson*, 1998]. Migmatites from the Fosdick Mountains yielded in situ U-Pb-Th monazite metamorphic ages as old as ~140 Ma [*Korhonen et al.*, 2010a, 2010b] and U-Pb zircon ages as old as 117 Ma [*McFadden et al.*, 2010]. Backarc plutonism accompanied extension, as represented by the alkalic Byrd Coast Granite in the Ford Ranges [*Adams*, 1987; *Weaver et al.*, 1992, 1994; *Muir et al.*, 1994; *Storey et al.*, 1999; *Mukasa and Dalziel*, 2000], from ca. 142–95 Ma [*Siddoway et al.*, 2004a]. These data suggest that regional heating coincided with the subduction-related calc-alkaline magmatism that is recorded by the main phase of the Median Batholith in New Zealand at ca. 145–120 Ma age [*Muir et al.*, 1997, 1998; *Mortimer et al.*, 1999; *Tulloch and Kimbrough*, 2003].

[9] In the Ford Ranges of western Marie Byrd Land, the geometry of faults and mafic dike arrays indicate that dextral transtension, associated with the West Antarctic Rift system, occurred in Cretaceous time. Contemporaneous mafic dikes [*Storey et al.*, 1999; *Siddoway et al.*, 2005] and brittle faults [*Luyendyk et al.*, 2003] strike NNW–SSE. The mafic dikes have $^{40}\text{Ar}/^{39}\text{Ar}$ ages of ca. 142–96 Ma [*Siddoway et al.*, 2005]. Crustal-scale, dextral strike-slip fault zones, inferred from airborne geophysics, strike E–W [*Ferraccioli et al.*, 2002; *Luyendyk et al.*, 2003].

[10] The Paleozoic rocks in the Ford Ranges are lower greenschist facies turbiditic sedimentary rocks (greywacke) of the Swanson Formation [*Wade et al.*, 1978; *Bradshaw et al.*, 1983; *Adams*, 1986] and the calc-alkaline Ford Granodiorite [*Pankhurst et al.*, 1998]. The association of Ford Granodiorite and Swanson Formation characterizes the Ross

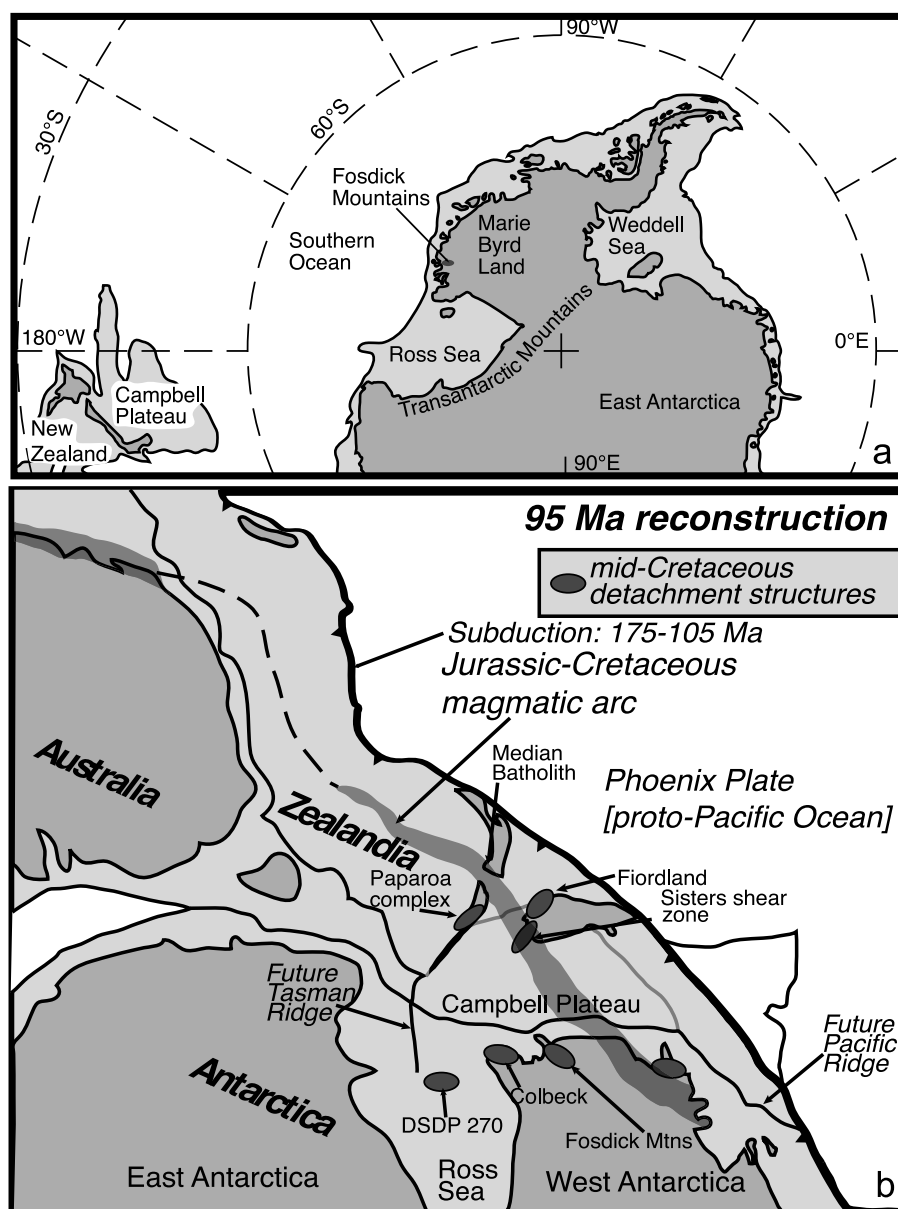


Figure 1. (a) Geographical map of Antarctica [after Pankhurst *et al.*, 1998]. (b) Tectonic plate reconstruction of the East Gondwana margin at 95 Ma, modified from Tulloch *et al.* [2006]. The locations of detachment structures are shown as dark gray ovals. The long axes of the ovals are parallel to the stretching direction in the detachments. Cape Colbeck [Siddoway *et al.*, 2004a]; DSDP 270 (Deep sea drill core): [Fitzgerald and Baldwin, 1997]; Paparoa complex [Tulloch and Kimbrough, 1989]; Fiordland [Gibson *et al.*, 1988; Scott and Cooper, 2006]; and Sisters Shear zone [Tulloch *et al.*, 2006; Kula *et al.*, 2007].

Province of West Antarctica [Pankhurst *et al.*, 1998]. Analogs in New Zealand are the Karamia Suite and Greenland Group [Tulloch *et al.*, 2009]. The sedimentary rocks were derived from the Ross-Delamerian and Lachlan Orogens, as evidenced by characteristic detrital zircon populations of ca. 500 to 450 Ma [Ireland *et al.*, 1998]. Ford Granodiorite is a calc-alkaline suite linked to Devonian-Carboniferous convergent margin plutonism at the border of East Gondwana. It intruded the Swanson Formation at

ca. 375 to 353 Ma, determined from Sr isotopes and zircon crystallization ages [Adams, 1986, 1987; Weaver *et al.*, 1992; Pankhurst *et al.*, 1998].

[11] Paragneisses and granodioritic orthogneisses in the Fostick migmatite-cored gneiss dome are the high temperature metamorphosed products of the Swanson Formation and the Ford Granodiorite, respectively [Siddoway and Fanning, 2009; Korhonen *et al.*, 2010a, 2010b]. The migmatites are a product of polyphase high temperature meta-

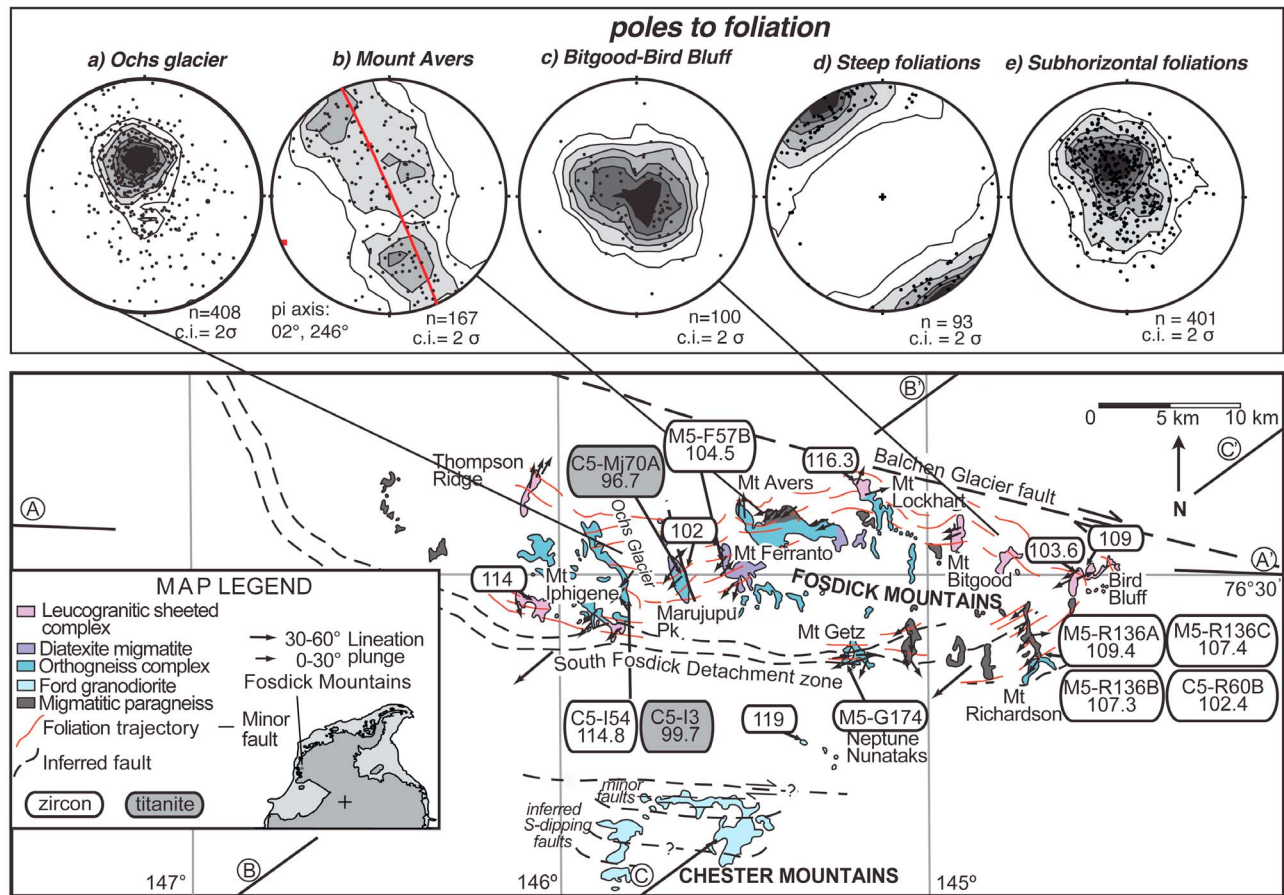


Figure 2. Geologic map of the Fosdick Mountains migmatite-cored gneiss dome and the Chester Mountains [after Siddoway *et al.*, 2004b]. The geographic location of the Fosdick Mountains in West Antarctica is shown in the map legend. The boundaries of the South Fosdick Detachment zone are shown as dashed lines, with arrows to represent the lineation trend for the zone. Long dashed lines represent mapped foliation trajectories. U-Pb SHRIMP ages are given for sample localities described in the text. A-A', B-B', and C-C' are the locations of the cross-sections in Figure 3. Stereographic projections with Kamb contours at a contour interval (c.i.) of 2σ are displayed. The projections summarize poles to foliation data from three geographic regions of the Fosdick Mountains and from two structural domains in the Fosdick Mountains: (a) Ochs glacier in the western portion, (b) Mount Avers in the central portion, (c) Bitgood to Bird Bluff in the eastern portion, (d) steep foliation domains, and (e) subhorizontal foliation domains. Equal area stereographic diagrams were made with Stereonet v.6.3.3, by Richard Allmendinger.

morphism. The Paleozoic phase experienced conditions of 820–870°C and 7–12 kb [Korhonen *et al.*, 2010a]. A second, major melting event occurred in the mid-Cretaceous at metamorphic conditions of 830–865°C and 6–7.5 kb, according to results of mineral equilibria modeling [Korhonen *et al.*, 2010a]. Sr-Nd isotopic and whole-rock major and trace element compositions indicate two types of Cretaceous granites, one derived from the Ford Granodiorite or a comparable plutonic source, and the other from meta-sedimentary sources, likely the Swanson Formation [Korhonen *et al.*, 2010b]. The granites derived from the Ford Granodiorite are consistently older than the granites derived from the Swanson Formation [Korhonen *et al.*, 2010b]. In addition, the Ford Granodiorite-derived gran-

ites are geochemically and temporally related to the Byrd Coast Granite in sites neighboring the Fosdick range consistent with studies in the broader Ford Ranges [Weaver *et al.*, 1991, 1992; Korhonen *et al.*, 2010b].

3. Fosdick Migmatite-Cored Gneiss Dome Architecture

[12] The Fosdick Mountains consist of Paleozoic and Cretaceous migmatitic paragneisses and orthogneisses and multiple types of granite emplaced as dikes, sills, and plutons. Microstructural observations of host gneisses indicate the former presence of melt and solid framework grains that

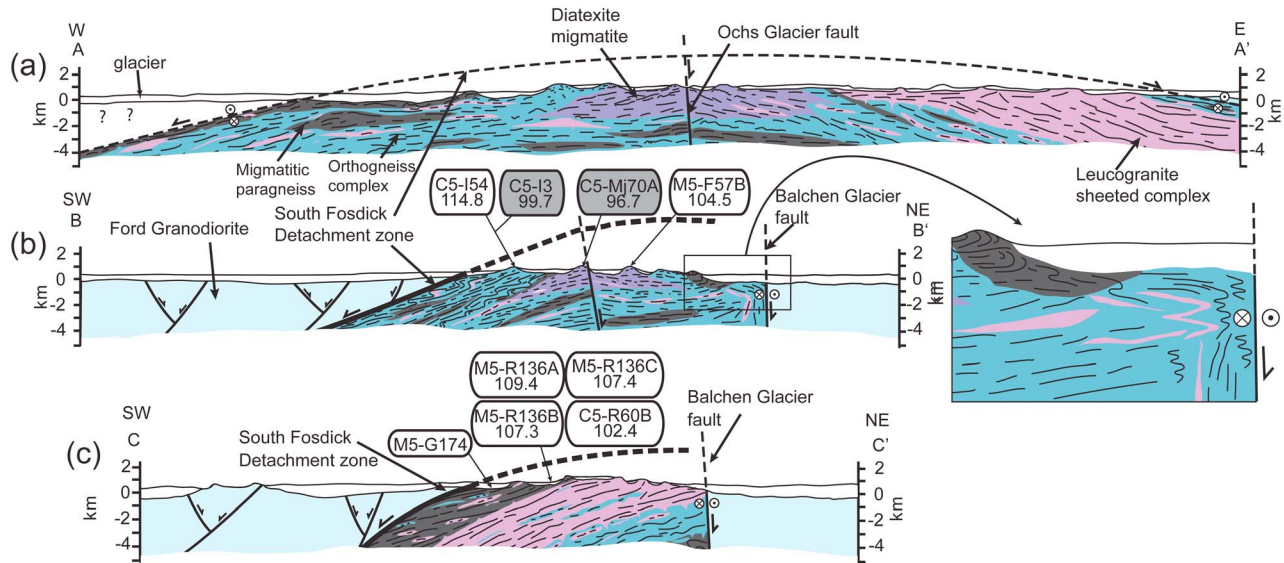


Figure 3. Geologic cross-sections of the Fosdick Mountains migmatite-cored gneiss dome. Scale: 1 cm = 5 km, with no vertical exaggeration. The migmatitic paragneiss (black) is the deepest unit, and forms thin layers and coherent blocks. The orthogneiss complex (dark gray) intruded the paragneisses and forms sub-horizontal layers. The diatexite migmatite unit (gray) forms a 1 km-thick section in the western portion of the dome. The leucogranite sheeted complex (light gray) outcrops predominantly in the eastern portion of the dome and forms an ~2 km-thick section that overlies the migmatitic paragneiss unit and orthogneiss complex. Ford Granodiorite (white) is a massive unit that forms the hanging wall of the Fosdick migmatite-cored gneiss dome. (a) Cross-section from A-A'. (b) Cross-section from B-B'. (c) Cross-section from C-C'. The enlarged portion of cross-section B-B' highlights the relationship between steep and subhorizontal fabrics in the Fosdick dome.

may have aided in the formation of a permeable network for melt flow [Siddoway *et al.*, 2004b; Siddoway and Fanning, 2009; Korhonen *et al.*, 2010a]. The leucosomes and granites are viewed as a remnant melt flow network through which an unknown volume of melt circulated [e.g., Brown, 2008] (migmatite terminology after Sawyer [2008]).

[13] In the Fosdick dome, the gneissic foliation defines a domal shape, with predominantly subhorizontal foliations (Figures 2 and 3) and NE–SW trending lineations and fold hinge lines. Subvertical to steeply dipping foliations are also found in the dome (Figure 3) within 100 m- to km-scale domains that are cut by, and partially to totally transposed into, zones of subhorizontal foliation [Siddoway *et al.*, 2004b]. The dome is bounded to the S by the South Fosdick Detachment zone, a shallowly S dipping, dextral oblique structure [McFadden *et al.*, 2007], and to the N by the Balchen Glacier fault, an inferred dextral strike-slip fault [Siddoway *et al.*, 2004b, 2005].

[14] The deepest level of the dome is an ~5 km-thick sequence of subhorizontal layers of migmatitic paragneiss and orthogneiss, and diatexite migmatite represented by the migmatitic paragneiss unit, orthogneiss complex, and diatexite unit (Figure 4). The gneisses host multiple generations of granite in discordant bodies, dikes, sills, and veins; they contain pervasively distributed leucosome (Figures 5a–5c). The orthogneiss and paragneiss layers are folded into km-scale recumbent folds. The folds pass upward into an

~2 km-thick section of subhorizontal leucogranite sheets with semi-concordant layers of m- to dm-scale paragneiss and orthogneiss (Figures 5d and 5e). Above the leucogranite sheeted complex is an ~1 km-thick section of migmatitic paragneiss and orthogneiss with leucosomes that have been sheared in the solid-state, associated with the South Fosdick Detachment zone [McFadden *et al.*, 2007].

3.1. Rock Units

3.1.1. Migmatitic Paragneiss

[15] Domains of refractory, residual paragneisses are exposed in the north-central (Mount Avers-type locality) and western portions of the Fosdick Range (Figures 2 and 3). The rocks are metatexite with cm- to dm-scale compositional layers alternating with m-thick layers of concordant garnet leucogranite (Figure 5a). The peak metamorphic assemblage in this unit is sillimanite + garnet + red-brown (titaniferous) biotite + ilmenite ± melt, determined from mineral equilibria modeling to have formed at temperatures of 820–870°C [Korhonen *et al.*, 2010a]. The garnet leucogranite is not internally foliated. The metatextitic paragneisses exhibit steep foliation that is folded into upright dm-scale folds (Figure 5a). Foliation, defined by the compositional layering, is folded about a SW-plunging π axis (oriented 02°, 246°) (Figure 2b). Mesoscopic fold hinges also trend NE–SW (oriented 15°, 244°) (Figure 4a). At

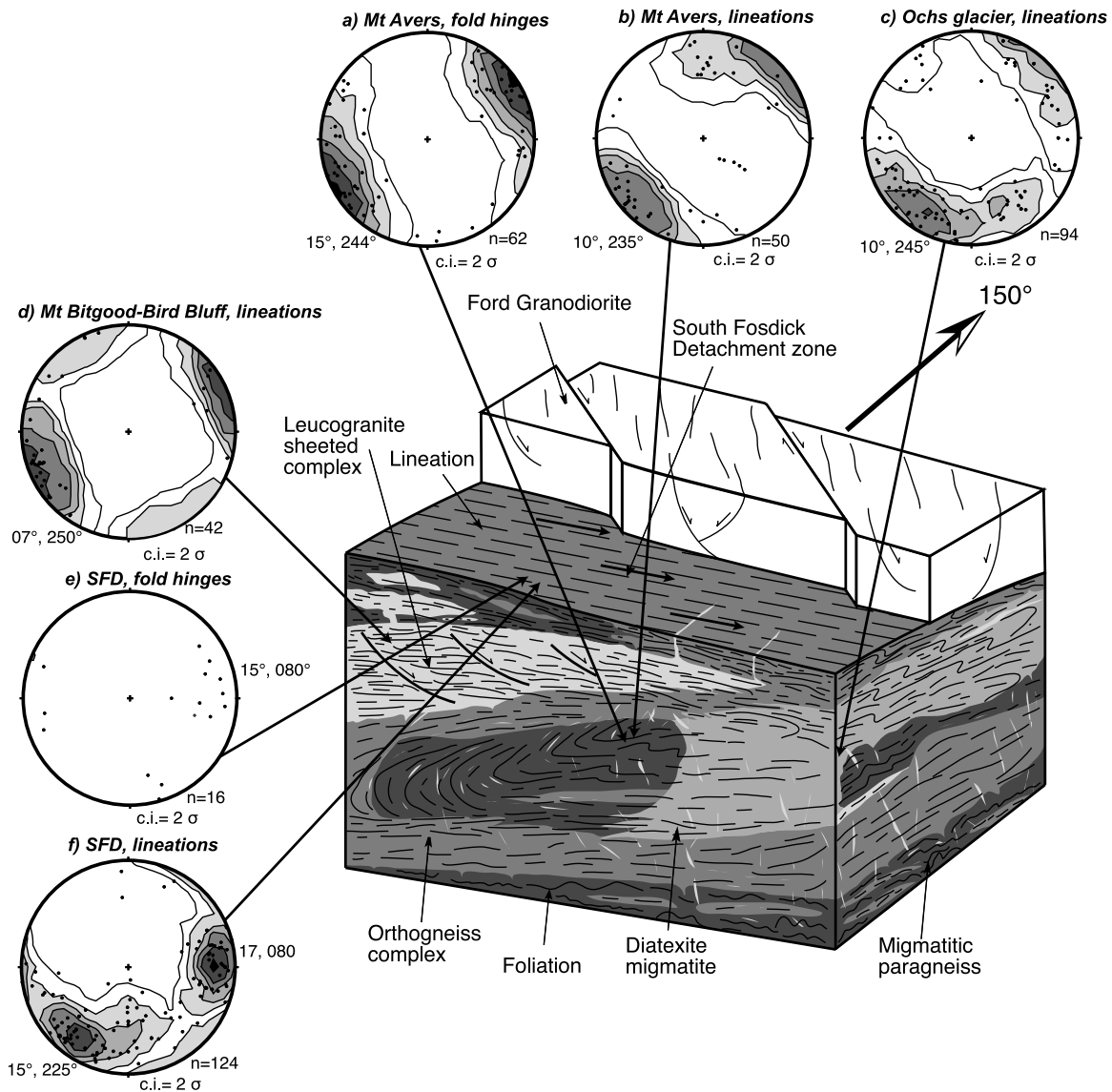


Figure 4. Schematic block diagram of the lithologic units and structures in the Fosdick migmatite-cored gneiss dome. Stereographic projections from the Fosdick migmatite-cored gneiss dome display data points and Kamb contours with a 2-σ contour interval. Symbols represent plotted field data as shown. (a) Fold hinges and determined pi axes from Mount Avers have a preferred NE–SW orientation (oriented 15°, 244°). (b) Mineral stretching lineations from Mount Avers have a similar NE–SW orientation (oriented 10°, 235°). (c) Mineral stretching lineations from the Ochs glacier region have considerable scatter, however, there is a dominant NE–SW orientation (oriented 10°, 245°). (d) Mineral stretching lineations from the Mount Bitgood-Bird Bluff region are less common, but where lineations occur they have sub-horizontal plunge and a NE–SW trend (oriented 07°, 250°). (e) Sparse fold hinges from the South Fosdick Detachment zone record an ENE–WSW trend (oriented 15°, 080°). (f) Mineral stretching lineations from the South Fosdick Detachment zone trend SW (oriented 15°, 225°). Crenulation lineations in the detachment zone have an ENE trend (oriented 17°, 080°). Equal area stereographic projections were made with Stereonet v.6.3.3., by Richard Allmendinger.

Mount Avers, the paragneiss forms a N-vergent, cylindrical km-scale fold nappe. In the migmatitic paragneiss at Mount Avers the dominant mineral stretching lineation trends SW (oriented 10°, 235°) and a secondary mineral stretching lineation trends N (Figure 4b).

3.1.2. Orthogneiss Complex

[16] The orthogneiss complex comprises ridges and summits in the north-central and western portions of the dome (Marujupu Peak, Mount Lockhart, Mount Avers, and Mount Iphigene) (Figures 2, 3, and 4). The orthogneiss complex is elsewhere referred to as a layered plutonic

complex [cf. *Siddoway and Fanning, 2009; Korhonen et al., 2010a*] because it consists of foliated, composite 10 m- to 100 m-thick sheets of orthogneiss and m- to dm-thick bodies of granite, granodiorite, and diorite, with minor, m- to 10 m-thick paragneiss layers (Figure 5b). Narrow, concordant leucosome layers and oblique, crosscutting granite networks transect the orthogneisses (Figure 5b). Folded, boudinaged, and disrupted amphibolite and diorite dikes and sills intrude the orthogneiss complex. In numerous locations, the disrupted and dismembered dikes form m-wide coherent blocks mantled by leucogranite (Figure 5b). The gneissic foliation dips gently to the SSE, folds are rare, and the mineral lineation is weak. Asymmetric fabrics and composite (C-S) fabrics give an inconsistent shear sense.

3.1.3. Diatexite Migmatite

[17] Diatexite migmatite and schollen-rich granite are exposed in the central portion of the Fosdick dome (Mount Ferranto, Marujupu Peak, and Mount Iphigene) (Figures 4 and 5c). The diatexite has a diffuse contact with the orthogneiss complex and the migmatitic paragneiss unit, and the diatexites display a faint foliation defined by biotite \pm garnet. Semi-concordant dm-scale paragneiss and orthogneiss layers are for the most part preserved, but the layers may be disrupted by agmatitic and schollen structures (Figure 5c). In the Ochs Glacier region, the diatexite migmatite unit reaches 1 km in thickness and has a shallow SSE dip (Figure 2a). In this unit, mineral stretching lineation

orientations are inconsistent, however, the dominant lineation trends SW (oriented 10° , 245°) (Figure 4c).

3.1.4. Leucogranite Sheeted Complex

[18] In the eastern (Mount Bitgood–Bird Bluff) and western portions of the Fosdick Mountains, subhorizontal leucogranite sheets overlie the migmatitic paragneiss unit and the orthogneiss complex (Figures 2, 3, and 4). The leucogranite sheeted complex consists of subhorizontal leucogranite sheets up to 100 m-thick that alternate with <1 to 10 m-thick layers of paragneiss and orthogneiss. In the eastern portion of the Fosdick dome, from Mount Bitgood to Bird Bluff, the leucogranite sheeted complex forms a composite 2 km-thick section (Figures 5d and 5e). The transition from the orthogneiss complex and the migmatitic paragneiss to the leucogranite sheeted complex is gradational and is defined by an increase in the proportion of leucogranite sheets.

[19] In the leucogranite sheeted complex, dm- to m-scale layers of paragneiss and orthogneiss exhibit subhorizontal foliation (Figure 2c). Foliation, defined by biotite and sillimanite [*Siddoway et al., 2004b*], is parallel to compositional layering defined by alternation of leucogranite sheets and intervening gneisses. The gneissic layers display tight to isoclinal recumbent folds, rootless, intrafolial folds, asymmetric inter-boudin partitions, and ellipsoidal blocks (Figures 5d and 5e). Subhorizontal mineral lineations trend SW (oriented 07° , 250°) (Figure 4d).

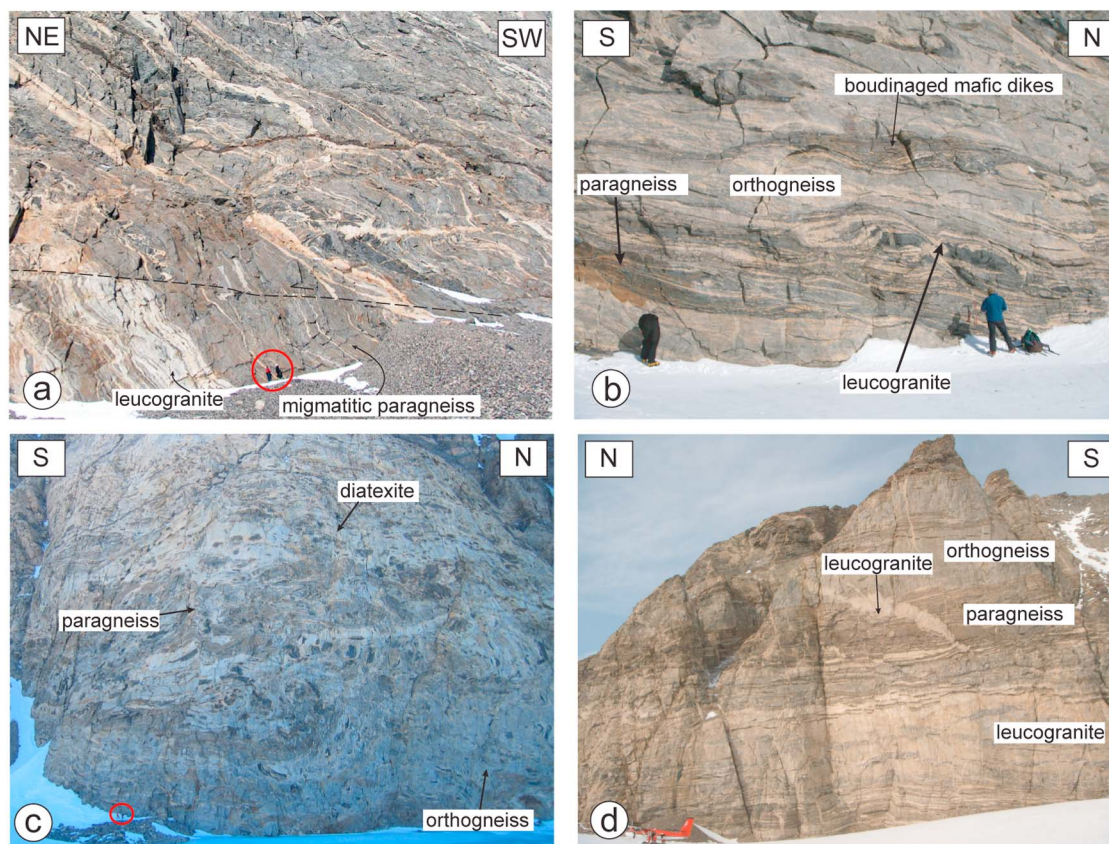


Figure 5

[20] Leucogranite and leucosome exist in diverse structural settings (Figure 5). At the 100 m- to km-scale, individual leucogranite sheets up to 100 m thick occur at lithologic contacts between units and along sheared fold limbs. At the dm- to m-scale, leucogranite is found in dikes and sills, inter-boudin regions, fold hinges, and shear zones (Figure 5b). Leucosomes are observed between foliated layers and within layers, arising as in situ leucosome, the crystallization product of anatectic melt that remained where it formed, and in-source leucosome, the crystallization product of anatectic melt that remained in the source layer, but migrated from the site of formation [e.g., *Sawyer, 2008*].

3.2. Structural Observations

3.2.1. Domains of Steep Foliation

[21] Steeply dipping to subvertical NE–SW striking foliations occur along the northern side of the Fosdick dome from Mount Iphigene to Mount Lockhart (Figure 2d). At Mount Ferranto, pronounced m-scale asymmetric, recumbent folds deform subvertical layers. Northern Mount Ferranto also preserves a steep, diffuse (10 m-wide) lithologic contact between migmatitic paragneiss and diatexite migmatite. The steep foliation domains exist primarily in the paragneiss and orthogneiss units, but at Mount Lockhart subvertical leucogranite sheets of the leucogranite sheeted complex exhibit steep foliation. Subvertical mafic dikes intrude the leucogranites, and both leucogranites and dikes

are folded. In the migmatitic paragneiss at Mount Lockhart, subhorizontal foliation crosscuts the subvertical layers (Figure 5f), and elsewhere, subhorizontal leucogranite sheets (Figure 5g) and subhorizontal, finely layered migmatitic paragneisses (Figure 5h) crosscut finely layered (mm- to cm-thick) migmatitic paragneiss with concordant leucosome. Isoclinal folds and transposed steep foliations have been documented at Mount Avers [*Siddoway et al., 2004b*]. In the steep domains, paragneiss and orthogneiss host multiple generations of leucosome, leucogranite dikes, granite sills, and dioritic dikes (Figure 6a).

3.2.2. Domains of Subhorizontal Foliation

[22] In the Fosdick dome, foliations in migmatite and granite are predominantly subhorizontal (Figure 2e). The subhorizontal fabrics commonly crosscut or transpose the steep fabrics and they are associated with NE–SW lineations and shallowly plunging microfolds [*Siddoway et al., 2004b*] (Figures 5f–5h). The diatexite migmatite unit forms a generally subhorizontal, composite 1 km-thick sheet in the central portion of the dome. In the leucogranite sheeted complex, leucogranite sheets and their internal foliation are parallel to the metamorphic layering. Trends of intrafolial fold hinge lines within the subhorizontal leucogranite sheeted complex are parallel with trends of recumbent fold hinge lines in the migmatite core [*Siddoway et al., 2004b*]. Within the subhorizontal domains, mafic dikes are recumbently folded and boudinaged, but are also found discordant to

Figure 5. Photos that display characteristic rock associations and structures from the lithologic units in the Fosdick migmatite-cored gneiss dome. (a) Photo of the migmatitic paragneiss unit (dark gray). The paragneisses display a steep foliation with dm- to m-scale folds. Garnet leucogranite layers (light gray) are interlayered with the paragneisses. The dashed line on the photo highlights a shallowly dipping reverse-sense shear band that crosscuts the migmatitic paragneiss unit. (b) Photo of the orthogneiss complex from the north-central portion of the dome (Mount Lockhart). Orthogneisses (gray) are interlayered with m-thick paragneiss layers (dark gray) and boudinaged mafic dikes (black). Cretaceous leucogranites (light gray) form cm- to dm-thick concordant layers and are emplaced in the inter-boudin regions and shear bands. (c) Photo of the diatexite migmatite unit exposed at Mount Iphigene. The diatexite migmatite unit contains semi-concordant folded and disrupted layers of orthogneiss (gray) and paragneiss (dark gray). Leucogranite veins (light gray to white) and leucosome transect the gneisses. The photo displays bodies of schollen-rich leucogranite and agmatitic diatexite with blocks of gneiss and dismembered mafic dikes surrounded by leucogranite. Where it is possible to observe a consistent fabric, biotite selvages and ghostly layers of gneiss define the foliation. Geologists at the base of the cliff are circled for scale. The cliff-face is ~500 m. Photo by S. C. Kruckenberg. (d) Photo of the leucogranite sheeted complex that displays a 50 m-thick subhorizontal leucogranite sheet (light gray) at Mount Bitgood. The leucogranite sheet intruded orthogneisses (gray) and paragneisses (dark gray) associated with the orthogneiss complex. A leucogranite dike with an irregular margin and leucogranite veins transect the orthogneiss and paragneiss layers. The dike is connected to concordant dm-thick leucogranite layers. Within the leucogranite sheet, dm-thick discontinuous orthogneiss layers define the foliation. Normal-sense shear bands that commonly host leucogranite offset the dominant gneissic foliation. The cliff is ~350 m in height. (e) Photo of the leucogranite sheeted complex at Bird Bluff. The subhorizontal 50 to 100 m-thick leucogranite sheets (light gray) intruded m- to dm-thick strongly deformed paragneiss (dark gray) and orthogneiss layers (gray). Crosscutting the compositional layering are outcrop-scale low angle normal-sense shear bands that commonly contain leucogranite. Mafic dikes (black) within leucogranite layers are boudinaged and folded. Blocks of disrupted dikes are generally elongate and parallel to the foliation. Geologists are circled for scale. Photo by F. McCarthy. The cliff-face is ~600 m. (f) Photo of a cliff-face of the migmatitic paragneiss unit from Mount Lockhart. The photo displays the subhorizontal foliation domain crosscutting the steep foliation domain. Both domains host concordant leucosome and leucogranite layers. Within the transition from steeply dipping foliation to subhorizontal foliation the layers form asymmetric recumbent folds. (g) Photo of migmatitic paragneiss and leucogranite from Mount Avers. The gneissic fabric, defined by cm-thick layers, is subvertical. The subvertical fabric is crosscut by a subhorizontal leucogranite that is interdigitated with the steep gneissic fabric. (h) Photo of a paragneiss layer from Mount Ferranto. Garnet-rich layers and mm- to cm-thick leucosome display a subvertical fabric that is crosscut by a transposed subhorizontal fabric defined by mm- to cm-thick leucosome. In the upper right portion of the photo, recumbently folded leucosomes are preserved.

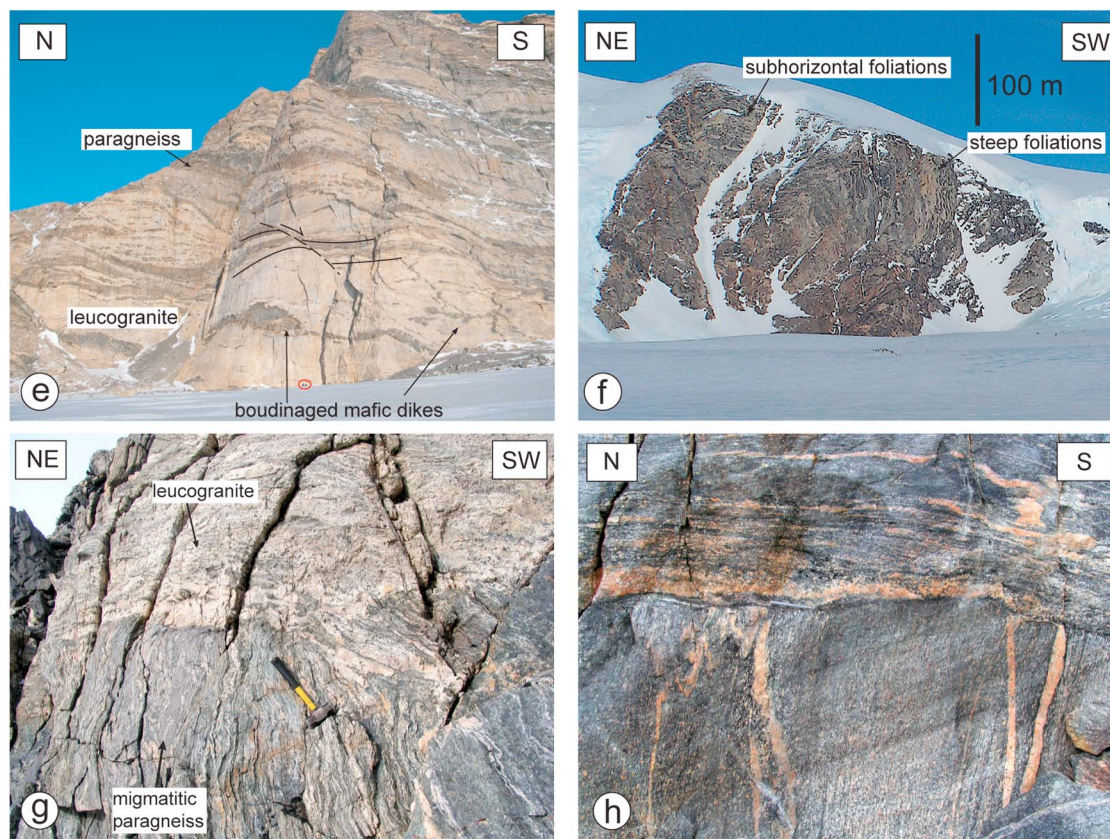


Figure 5. (continued)

the gneissic fabric [Smith, 1997; McFadden *et al.*, 2010] (Figure 6b).

3.2.3. South Fosdick Detachment Zone

[23] The South Fosdick Detachment zone is an ~1 km-thick zone of solid-state deformed gneisses preserved in ridges along the S flank of the Fosdick range [McFadden *et al.*, 2007] (Figures 2, 3, and 4). Foliation in the detachment zone generally dips 20 to 30° to the S, but at Mount Richardson the dips reach 70°. Penetrative foliation and lineation are defined by stretched quartz, biotite, and sillimanite (Figure 6f). The dominant mineral stretching lineation trends SW (oriented 15°, 225°) and an overprinting crenulation lineation trends E (oriented 07°, 080°) (Figure 4f). Asymmetric feldspar porphyroclasts and C-S fabrics record top-to-the-SW oblique motion [McFadden *et al.*, 2007]. Meter-scale, open, upright, low amplitude folds (corrugations) with fold hinge lines sub-parallel to the 080° crenulation lineation deform the detachment foliation (Figure 4e).

[24] In the eastern Fosdick Mountains, from Bird Bluff to Mount Richardson, there is a gradational boundary between the leucogranite sheeted complex and the South Fosdick Detachment zone (Figures 2 and 3), corresponding to a decrease in the proportion of leucogranite sheets and an increase in the proportion of paragneiss and orthogneiss layers that exhibit solid-state deformation. The paragneiss and orthogneiss host concordant, mm- to cm-scale in-source

leucosome, poorly developed discordant leucosome, and granite veins (Figures 6c and 6d). The paragneiss and orthogneiss layers contain microstructures indicative of the former presence of melt [McFadden *et al.*, 2007; Siddoway *et al.*, 2008]. A tabular leucogranite body, associated with the leucogranite sheeted complex, intruded the South Fosdick Detachment zone and preserves magmatic flow fabrics that are defined by passively folded late mafic dikes (Figure 6e). The folded mafic dikes are interpreted to be deformed by flow folds based on attenuation of thin, sheared limbs and thickening within wide fold hinges with irregular margins. The margins of the tabular leucogranite body are interdigitated with the gneissic foliation and are interfoliated with the migmatites, which we interpret as evidence of syntectonic emplacement. Leucogranite dikes and veins connected with the tabular leucogranite are intercalated with paragneiss and orthogneiss layers. The leucogranites occupy extensional structures such as inter-boudin partitions and shear bands (Figures 6c and 6d). In the central portion of the detachment zone (Mount Getz), a late granitic dike, associated with a granitic sill, crosscuts the solid-state deformation preserved in paragneiss layers (Figure 6f).

3.2.4. Late Structures

[25] Late- to post-tectonic structures that do not contain evidence for significant extension crosscut the detachment zone and all rock units. These structures include, in older

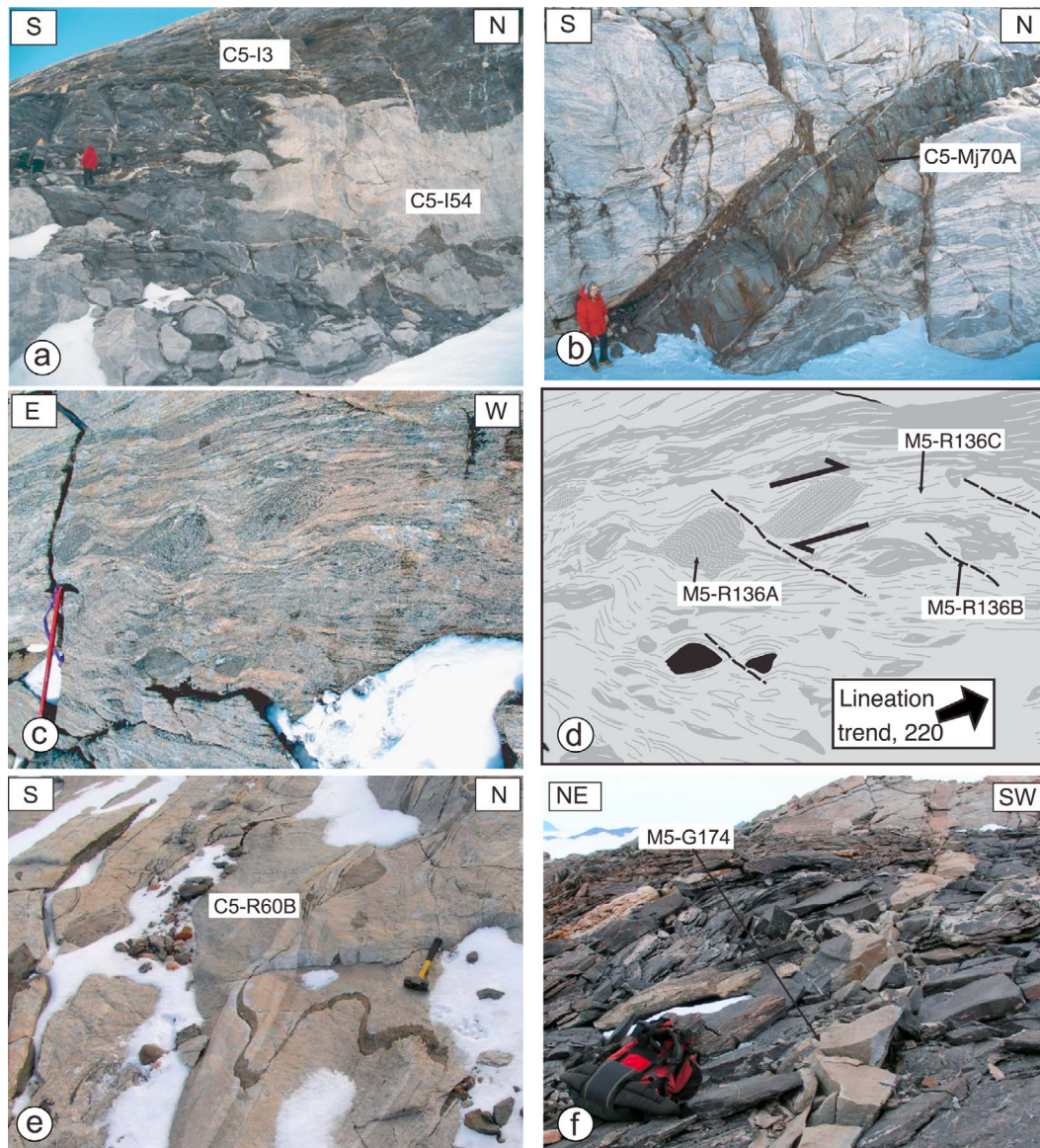


Figure 6. Field photos of samples presented for U-Pb SHRIMP geochronology. (a) Diorite dike that cuts across compositional layering and foliation, but is folded and interdigitated with neighboring granite. Zircon sample C5-I54 comes from the granite and titanite sample C5-I3 is from the diorite dike. (b) Diorite dikes that cut the diatexite migmatite of Marujupu Peak. The photo displays two dikes. The narrower dike on top is in contact with the main, thicker dike. The narrower dike has numerous granitic xenoliths and after running parallel to the main dike, it deviates at a sharp bend. Titanite sample C5-Mj70A was collected from the main, thicker dike. Leucogranite veins intrude the thicker dike. In addition, the thicker dike has irregular margins that are incorporated in the gneissic foliation. (c–d) Photo and sketch of the U-Pb zircon sample locality at Mount Richardson for samples M5-R136A, M5-R136C, and M5-R136B. Biotite granodiorite orthogneiss that forms sigmoidal boudins that indicate top-to-the-SW normal oblique shear sense. Leucogranite forms concordant layers and exists in inter-boudin regions and shear bands. (e) Photo of the tabular leucogranite body, sample C5-R60B, that intrudes the South Fosdick Detachment zone. Late magmatic mafic dikes define disharmonic folds and indicate passive folding during flow of the seemingly undeformed host leucogranite. The fold limbs are sheared and thin, whereas the fold hinges are wide and have irregular boundaries. (f) Crosscutting granitic dike, sample M5-G174, that is connected to a wider granite sill at Mount Getz. The dike has a weak magmatic fabric and crosscuts paragneiss with a solid-state fabric imparted by the South Fosdick Detachment zone.

to younger sequence based on crosscutting relationships: 1) normal-sense, moderately S- and N-dipping anatectic granite-filled shear bands cutting across metamorphic foliation and folds [Richard, 1992; Siddoway *et al.*, 2004b], 2) subvertical, discordant leucocratic veins and mafic dikes [Siddoway *et al.*, 2005] (Figure 6b), 3) muscovite-coated brittle fractures [Richard, 1992], and 4) brittle normal-sense shears [McFadden *et al.*, 2007]. The structures strike approximately E–W and record approximately N–S stretching.

4. U-Pb Geochronology Sampling Strategy

[26] SHRIMP U-Pb zircon and titanite analyses are used to address the temporal relationship between magma accumulation and oblique extensional deformation. U-Pb zircon samples are from granite and leucosome hosted within steep foliation domains and granite and leucosome hosted within subhorizontal foliation domains or within the South Fosdick Detachment zone (Figures 2, 3, and 6). U-Pb titanite samples are from late- to post-tectonic diorite dikes. One is folded with the gneissic foliation and leucogranite, and the other crosscuts the subhorizontal gneissic foliation (Figures 2, 3, and 6). Titanite from the diorite dikes was analyzed because the dikes do not contain zircon.

4.1. Steep Domains

[27] In order to document the timing of granite emplacement in the steep foliation domains, a folded, biotite granite sheet from the orthogneiss complex on southern Mount Iphigene was sampled (C5-I54) (Figure 6a). The granite sheet is medium-grained and hypidiomorphic, and it is commingled with a diorite dike. For comparison, age data are presented from a folded, steeply dipping 2 m-thick leucogranite sill (M6-L188) from within the leucogranite sheeted complex on Mount Lockhart [McFadden *et al.*, 2010] and from a granite emplaced in steep foliation from Mutel Peak [Korhonen *et al.*, 2010a].

4.2. Subhorizontal Domains and the South Fosdick Detachment Zone

[28] Granites emplaced in subhorizontal domains and granites emplaced within the South Fosdick Detachment zone were sampled in an attempt to define the timing of subhorizontal foliation development and solid-state deformation in the detachment zone. A concordant, subhorizontal, 20 cm-thick, coarse-grained granite sill from within the diatexite migmatite of Mount Ferranto was sampled (M5-F57B). A subhorizontal leucogranite sheet (C6-BB112) and a subhorizontal granite body (K6-Bb47) from within the leucogranite sheeted complex on Bird Bluff were sampled and results are presented by [McFadden *et al.*, 2010] and [Korhonen *et al.*, 2010a], respectively. [Korhonen *et al.*, 2010a] also presented age data on a subhorizontal, 1 m-thick granite sill from Marujupu Peak.

[29] Samples from the eastern portion of the detachment zone at Mount Richardson offer crosscutting relationships for a relative chronology. The four samples in order of relative age are: a boudinaged, medium-grained granodioritic orthogneiss (M5-R136A) (Figures 6c and 6d); a

10 cm-wide granite sill concordant to the gneissic foliation (M5-R136C) (Figures 6c and 6d); an equigranular biotite granite from a discordant dextral normal shear band (M5-R136B) (Figures 6c and 6d); and a 100 m-wide tabular, concordant leucogranite sheet that intruded the gneissic foliation and has margins interdigitated with the gneissic foliation. It preserves a magmatic foliation (C5-R60B) (Figure 6e). A U-Pb sample from the central portion of the detachment zone at Mount Getz is an equigranular medium-grained two-mica granite dike that crosscuts the gneissic foliation and displays a weak magmatic fabric (M5-G174) (Figure 6f). The dike is associated with a larger granitic sill.

4.3. Late- to Post-Tectonic Dikes

[30] Two diorite dikes that are folded within or crosscut the gneissic foliation in the Ochs Glacier region were sampled for SHRIMP U-Pb titanite analyses in an effort to constrain a minimum age for the development of the Fosdick dome gneissic foliation. Sample C5-I3 is an ~10 m-wide, medium-grained diorite dike that intruded the paragneiss and granite (C5-I54) on southern Mount Iphigene (Figure 6a). The diorite dike is recumbently folded together with the granite and surrounding gneisses. The diorite-granite contact is interdigitated along the foliation. Cm-wide aplitic veins crosscut the diorite. Subhedral to euhedral titanite grains 1–2 mm in dimension are evenly distributed throughout the diorite. The second sample was taken from a post-tectonic, tabular dike that crosscuts the gneissic foliation within the diatexite migmatite unit on Marujupu Peak (C5-Mj70A) (Figure 6b). It is an ~2 m-thick medium-grained diorite dike that dips moderately to the SW, with planar discordant contacts and no internal foliation. Visible igneous titanites of 0.3 to 1 mm in length are evenly distributed throughout the diorite.

5. U-Pb Geochronology

5.1. Analytical Procedure

[31] Zircon mineral separates were prepared from bulk rock samples by crushing, gravity and magnetic separation, heavy liquids, and hand picking at the Australian National University Research School of Earth Sciences. Zircons were mounted in epoxy, ground to approximately half-thickness, and polished with 3 μm and 1 μm diamond paste. Due to the coarse grain size of titanite in diorite samples, titanite mineral separates were prepared by crushing and hand picking at Colorado College. All grains were imaged in transmitted and reflected light on a petrographic microscope. Zircons were imaged using cathodoluminescence (CL) on a scanning electron microscope (SEM) and titanites were imaged using backscattered secondary electrons (BSE) on the SEM. Zircon grains were analyzed using SHRIMP II and titanite grains were analyzed using SHRIMP RG at the Research School of Earth Sciences, Australian National University. Procedures are as given by [Williams, 1998]. Data were reduced using the SQUID Excel Macro of [Ludwig, 2001]. The zircon U/Pb ratios have been normalized relative to a value of 0.0668 for the Temora reference zircon, equivalent to an age of 417 Ma [Black *et al.*, 2003].

Table 1. Summary of SHRIMP U-Pb Zircon Results for Granites and Leucosome in the Fosdick Mountains^a

Grain Spot	U (ppm)	Th (ppm)	Th/U	²⁰⁶ Pb ^b (ppm)	²⁰⁴ Pb/ ²⁰⁶ Pb	f ₂₀₆ ^c (%)	Total ²³⁸ U/ ²⁰⁶ Pb	Error ^d	²⁰⁷ Pb/ ²⁰⁶ Pb	Error ^d	Radiogenic Ratios		Age (Ma)	
											²⁰⁶ Pb/ ²³⁸ U	Error ^d	²⁰⁶ Pb/ ²³⁸ U	Error ^d
Sample C5-I54 (location: S 76° 32.318, W 145° 51.061) ^{e,f}														
Rims														
1.1	2626	592	0.23	40.4	0.000044	0.22	55.891	0.586	0.0501	0.0004	0.0179	0.0002	114.1	1.2
2.1	1887	73	0.04	275.2	0.000000	0.36	5.892	0.068	0.0757	0.0002	0.1691	0.0020	1007.3	11.2
3.1	1001	206	0.21	14.8	0.000239	0.78	57.981	0.630	0.0544	0.0006	0.0171	0.0002	109.4	1.2
4.1	2039	281	0.14	169.3	0.000018	5.46	10.349	0.163	0.1034	0.0005	0.0913	0.0015	563.5	8.7
5.1	1225	227	0.19	19.1	0.000072	0.30	55.230	0.593	0.0507	0.0005	0.0181	0.0002	115.3	1.2
8.1	2542	472	0.19	38.7	0.000013	0.23	56.465	0.588	0.0501	0.0004	0.0177	0.0002	112.9	1.2
9.1	954	8	0.01	14.7	0.000068	0.37	55.865	0.685	0.0513	0.0006	0.0178	0.0002	113.9	1.4
10.1	1375	130	0.09	66.7	0.000028	0.29	17.714	0.217	0.0559	0.0005	0.0563	0.0007	353.0	4.2
11.1	1864	482	0.26	29.0	0.000040	0.33	55.270	0.587	0.0510	0.0006	0.0180	0.0002	115.2	1.2
12.1	1769	8	0.00	28.0	0.000037	0.15	54.346	0.573	0.0496	0.0004	0.0184	0.0002	117.4	1.2
14.1	2448	183	0.07	36.5	0.000181	0.56	57.572	0.601	0.0527	0.0004	0.0173	0.0002	110.4	1.1
15.1	1504	297	0.20	23.5	0.000265	0.16	54.975	0.589	0.0496	0.0005	0.0182	0.0002	116.0	1.2
16.1	2859	540	0.19	45.7	0.000049	<0.01	53.701	0.562	0.0480	0.0003	0.0186	0.0002	119.0	1.2
17.1	772	101	0.13	11.7	0.000193	0.19	56.642	0.630	0.0498	0.0007	0.0176	0.0002	112.6	1.2
18.1	957	368	0.39	15.7	0.000011	0.09	52.368	0.584	0.0491	0.0008	0.0191	0.0002	121.8	1.4
19.1	300	268	0.89	4.4	-	0.54	59.163	0.732	0.0524	0.0012	0.0168	0.0002	107.5	1.3
20.1	2426	237	0.10	38.1	0.000603	1.14	54.685	0.578	0.0574	0.0004	0.0181	0.0002	115.5	1.2
21.1	376	22	0.06	37.9	0.000040	2.00	8.520	0.247	0.0793	0.0053	0.1150	0.0035	701.8	20.3
Cores														
6.1	2732	279	0.10	41.6	0.000033	0.19	56.370	0.643	0.0498	0.0003	0.0177	0.0002	113.1	1.3
7.1	932	212	0.23	14.6	0.000049	0.26	54.718	0.590	0.0504	0.0006	0.0182	0.0002	116.4	1.3
9.2	129	26	0.20	9.7	0.000235	0.48	11.476	0.174	0.0621	0.0008	0.0867	0.0013	536.1	8.0
13.1	1962	347	0.18	31.8	0.000020	0.24	52.954	0.605	0.0503	0.0004	0.0188	0.0002	120.3	1.4
14.2	275	112	0.41	23.1	0.000135	0.06	10.225	0.120	0.0604	0.0006	0.0977	0.0012	601.2	6.9
20.2	1845	331	0.18	164.8	-	<0.01	9.617	0.114	0.0599	0.0005	0.1041	0.0013	638.5	7.4
Sample M5-F57B (location: S 76° 29.734, W 145° 32.153) ^{g,h}														
Rims														
2.1	2291	67	0.029	33.4	0.000424	0.64	58.901	0.625	0.0532	0.0005	0.0169	0.0002	107.8	1.1
3.1	1178	23	0.020	16.8	0.001507	2.75	60.112	0.669	0.0699	0.0012	0.0162	0.0002	103.5	1.2
4.1	1570	37	0.023	22.7	0.001265	1.89	59.438	0.646	0.0632	0.0007	0.0165	0.0002	105.5	1.1
5.1	1572	16	0.010	23.9	0.000910	1.75	56.421	0.612	0.0622	0.0014	0.0174	0.0002	111.3	1.2
6.1	1094	17	0.016	15.4	0.000713	1.38	61.018	0.686	0.0591	0.0009	0.0162	0.0002	103.4	1.2
7.1	1564	38	0.024	21.9	0.001028	1.65	61.294	0.669	0.0612	0.0007	0.0160	0.0002	102.6	1.1
8.1	1258	19	0.015	17.7	0.000350	0.93	60.910	0.689	0.0555	0.0008	0.0163	0.0002	104.0	1.2
9.1	1419	35	0.025	20.1	0.000362	0.46	60.667	0.666	0.0518	0.0007	0.0164	0.0002	104.9	1.1
10.1	1401	29	0.020	20.2	0.000696	1.01	59.680	0.657	0.0561	0.0007	0.0166	0.0002	106.1	1.2
11.1	1457	8	0.005	21.4	0.000432	0.88	58.580	0.642	0.0551	0.0007	0.0169	0.0002	108.2	1.2
12.1	1215	18	0.015	17.9	0.002257	3.70	58.436	0.652	0.0775	0.0011	0.0165	0.0002	105.4	1.2
13.1	1109	9	0.008	16.1	0.000579	0.84	59.137	0.680	0.0548	0.0009	0.0168	0.0002	107.2	1.2
14.1	1629	43	0.027	23.0	0.000409	0.57	60.967	0.667	0.0526	0.0007	0.0163	0.0002	104.3	1.1
15.1	1277	26	0.020	18.3	0.000569	1.08	60.064	0.680	0.0567	0.0012	0.0165	0.0002	105.3	1.2
Cores														
1.1	1280	8	0.006	20.8	0.001104	2.59	52.921	1.362	0.0690	0.0027	0.0184	0.0005	117.6	3.0
Sample M5-R136A (location: S 76° 32.877, W 144° 41.248) ^{g,i}														
Rims														
1.1	3143	218	0.069	46.2	0.000167	0.36	58.495	0.605	0.0510	0.0006	0.0170	0.0002	108.9	1.1
2.1	3082	94	0.031	45.4	0.000360	0.88	58.279	0.597	0.0552	0.0007	0.0170	0.0002	108.7	1.1
3.1	692	344	0.496	10.3	0.000648	0.90	57.545	0.641	0.0554	0.0009	0.0172	0.0002	110.1	1.2
5.1	1500	50	0.033	75.4	0.000047	0.19	17.105	0.193	0.0554	0.0004	0.0584	0.0007	365.6	4.1
6.1	1307	31	0.023	19.2	0.000408	0.61	58.350	0.642	0.0530	0.0007	0.0170	0.0002	108.9	1.2
7.1	1646	17	0.011	22.7	0.000075	0.24	62.314	0.677	0.0500	0.0007	0.0160	0.0002	102.4	1.1
9.1	163	59	0.364	2.5	0.000998	3.04	56.981	0.920	0.0723	0.0025	0.0170	0.0003	108.8	1.8
10.1	658	30	0.045	9.7	0.001136	0.69	57.958	0.688	0.0537	0.0010	0.0171	0.0002	109.5	1.3
11.1	2484	14	0.006	34.7	0.000191	0.38	61.456	0.652	0.0511	0.0007	0.0162	0.0002	103.7	1.1
12.1	1407	417	0.296	20.3	0.000143	0.35	59.519	0.654	0.0509	0.0007	0.0167	0.0002	107.0	1.2
13.1	1341	50	0.037	18.9	0.000343	0.57	61.079	0.675	0.0526	0.0007	0.0163	0.0002	104.1	1.1
15.1	1380	19	0.014	19.1	0.000405	0.73	62.163	0.687	0.0539	0.0008	0.0160	0.0002	102.1	1.1
16.1	3099	47	0.015	46.4	0.000183	0.29	57.378	0.643	0.0506	0.0007	0.0174	0.0002	111.1	1.2
17.1	2219	38	0.017	31.5	0.000177	0.40	60.445	0.702	0.0513	0.0006	0.0165	0.0002	105.4	1.2
18.1	2813	443	0.158	40.3	0.000173	0.55	59.930	0.638	0.0525	0.0005	0.0166	0.0002	106.1	1.1
19.1	1517	23	0.015	21.6	0.000137	0.60	60.214	0.658	0.0529	0.0007	0.0165	0.0002	105.5	1.2
20.1	2624	599	0.228	37.8	0.000123	0.26	59.688	0.637	0.0502	0.0005	0.0167	0.0002	106.8	1.1
21.1	1372	20	0.014	19.7	0.000166	0.27	59.935	0.658	0.0503	0.0007	0.0166	0.0002	106.4	1.2
22.1	1732	28	0.016	25.3	0.000391	0.98	58.841	0.638	0.0560	0.0008	0.0168	0.0002	107.6	1.2

Table 1. (continued)

Grain Spot	U (ppm)	Th (ppm)	Th/U	²⁰⁶ Pb ^b (ppm)	²⁰⁴ Pb/ ²⁰⁶ Pb	f ₂₀₆ ^c (%)	Total ²³⁸ U/ ²⁰⁶ Pb	Error ^d	²⁰⁷ Pb/ ²⁰⁶ Pb	Error ^d	Radiogenic Ratios		Age (Ma)	
											²⁰⁶ Pb/ ²³⁸ U	Error ^d	²⁰⁶ Pb/ ²³⁸ U	Error ^d
Cores														
1.2	895	174	0.194	13.4	0.000262	0.47	57.355	0.613	0.0520	0.0006	0.0174	0.0002	110.9	1.2
2.2	384	95	0.247	17.3	0.000234	0.30	19.100	0.222	0.0554	0.0006	0.0522	0.0006	328.0	3.8
4.1	446	137	0.307	22.7	0.000276	0.62	16.879	0.183	0.0590	0.0006	0.0589	0.0006	368.8	3.9
4.2	122	1	0.010	9.9	0.000752	1.54	10.631	0.141	0.0717	0.0011	0.0926	0.0013	571.0	7.4
7.2	414	173	0.419	6.1	0.001588	1.00	58.175	0.791	0.0562	0.0016	0.0170	0.0002	108.8	1.5
8.1	470	43	0.092	17.3	0.000179	0.66	23.304	0.267	0.0569	0.0008	0.0426	0.0005	269.1	3.1
14.1	271	97	0.360	13.4	0.000395	1.12	17.355	0.210	0.0627	0.0010	0.0570	0.0007	357.2	4.3
17.2	2418	1753	0.725	35.2	0.001532	2.59	58.952	0.632	0.0687	0.0032	0.0165	0.0002	105.7	1.2
23.1	1304	706	0.542	43.5	0.061008	35.30	25.784	2.056	0.3307	0.1507				
24.1	393	43	0.110	12.9	0.000700	0.80	26.105	0.322	0.0574	0.0015	0.0380	0.0005	240.4	3.0
25.1	198	180	0.910	9.9	0.000434	0.92	17.166	0.232	0.0612	0.0013	0.0577	0.0008	361.7	4.8
26.1	990	731	0.739	50.0	0.000056	0.09	17.016	0.185	0.0546	0.0007	0.0587	0.0006	367.8	3.9
Sample M5-R136C (location: S 76° 32.877, W 144° 41.248) ^{g,j}														
Rims														
1.1	889	45	0.051	44.4	0.000007	0.17	17.187	0.201	0.0552	0.0005	0.0581	0.0007	364.0	4.2
3.1	2376	21	0.009	32.7	-	0.09	62.365	0.667	0.0488	0.0006	0.0160	0.0002	102.5	1.1
4.1	536	195	0.363	7.7	0.000249	0.05	59.453	0.740	0.0486	0.0012	0.0168	0.0002	107.5	1.3
5.1	2748	71	0.026	39.8	-	0.09	59.329	0.625	0.0489	0.0005	0.0168	0.0002	107.7	1.1
6.1	3372	49	0.014	49.3	0.001594	2.55	58.811	0.615	0.0684	0.0005	0.0166	0.0002	105.9	1.1
7.1	1342	24	0.018	18.8	0.000164	0.33	61.343	0.674	0.0507	0.0007	0.0162	0.0002	103.9	1.1
8.2	2066	53	0.026	107.4	-	<0.01	16.535	0.172	0.0541	0.0003	0.0605	0.0006	378.6	3.9
9.1	1001	23	0.023	14.3	0.000179	<0.01	60.172	0.679	0.0480	0.0008	0.0166	0.0002	106.3	1.2
10.1	2804	11	0.004	40.3	-	<0.01	59.764	0.635	0.0481	0.0005	0.0167	0.0002	107.0	1.1
11.1	2254	17	0.008	32.3	-	0.01	59.995	0.645	0.0482	0.0005	0.0167	0.0002	106.6	1.1
12.1	1524	492	0.323	61.1	-	0.12	21.427	0.225	0.0532	0.0004	0.0466	0.0005	293.7	3.0
Cores														
1.2	785	230	0.293	36.0	0.000046	0.21	18.713	0.202	0.0549	0.0005	0.0533	0.0006	334.9	3.6
2.1	1305	34	0.026	67.4	-	<0.01	16.624	0.274	0.0530	0.0004	0.0602	0.0010	377.1	6.1
3.2	628	327	0.520	9.0	0.000350	0.42	59.652	0.759	0.0515	0.0013	0.0167	0.0002	106.7	1.4
6.2	953	587	0.616	48.4	0.000031	0.03	16.901	0.184	0.0543	0.0005	0.0591	0.0007	370.5	4.0
8.1	188	75	0.402	9.4	-	0.47	17.150	0.228	0.0576	0.0012	0.0580	0.0008	363.7	4.8
9.2	611	340	0.556	9.0	0.000321	0.08	58.604	0.724	0.0488	0.0011	0.0171	0.0002	109.0	1.3
10.2	395	197	0.499	5.8	-	0.17	58.949	0.761	0.0496	0.0013	0.0169	0.0002	108.3	1.4
13.1	568	90	0.159	10.1	0.000022	0.20	48.170	0.599	0.0503	0.0014	0.0207	0.0003	132.2	1.6
14.1	450	144	0.321	22.1	0.000259	0.03	17.498	0.205	0.0539	0.0008	0.0571	0.0007	358.2	4.1
15.1	1331	418	0.314	19.7	0.000171	0.09	58.000	0.659	0.0490	0.0009	0.0172	0.0002	110.1	1.2
16.1	750	342	0.457	11.0	-	<0.01	58.784	0.717	0.0471	0.0011	0.0170	0.0002	108.9	1.3
17.1	607	251	0.414	8.8	0.000202	0.12	59.472	0.754	0.0491	0.0012	0.0168	0.0002	107.4	1.4
18.1	1300	693	0.533	19.0	-	0.03	58.875	0.670	0.0484	0.0008	0.0170	0.0002	108.5	1.2
19.1	1059	652	0.615	53.3	0.000069	0.08	17.059	0.184	0.0546	0.0005	0.0586	0.0006	366.9	3.9
Sample M5-R136B (location S 76° 32.877, W 144° 41.248) ^{g,k}														
Rims														
1.1	3773	201	0.053	56.1	0.003071	5.44	57.796	0.602	0.0913	0.0022	0.0164	0.0002	104.6	1.1
2.1	1958	23	0.012	29.4	-	0.03	57.275	0.616	0.0485	0.0006	0.0175	0.0002	111.5	1.2
3.1	1743	44	0.025	25.2	0.000250	0.24	59.479	0.641	0.0501	0.0006	0.0168	0.0002	107.2	1.2
4.1	1676	45	0.027	24.1	-	0.15	59.793	0.659	0.0494	0.0006	0.0167	0.0002	106.8	1.2
Cores														
1.2	1043	474	0.455	15.2	-	0.13	59.139	0.677	0.0492	0.0009	0.0169	0.0002	108.0	1.2
4.2	1739	1068	0.614	25.0	0.000305	0.79	59.688	0.651	0.0544	0.0007	0.0166	0.0002	106.3	1.2
5.1	1730	1129	0.652	25.2	-	0.10	59.008	0.649	0.0490	0.0007	0.0169	0.0002	108.2	1.2
6.1	355	299	0.843	5.1	-	0.02	59.995	0.837	0.0483	0.0016	0.0167	0.0002	106.5	1.5
7.1	645	206	0.320	71.9	0.000024	0.55	7.708	0.150	0.0698	0.0005	0.1290	0.0026	782	15
8.1	553	196	0.355	8.8	-	0.10	54.102	0.946	0.0492	0.0012	0.0185	0.0003	118.0	2.1
9.1	2072	1490	0.719	31.3	0.000072	0.07	56.942	0.617	0.0489	0.0006	0.0175	0.0002	112.1	1.2
10.1	345	165	0.478	5.0	-	0.26	58.847	0.833	0.0503	0.0017	0.0169	0.0002	108.3	1.5
11.1	588	364	0.619	8.4	0.000301	<0.01	59.873	0.758	0.0477	0.0012	0.0167	0.0002	106.8	1.4
12.1	854	511	0.598	12.3	0.000219	0.29	59.898	0.713	0.0504	0.0010	0.0166	0.0002	106.4	1.3
13.1	726	309	0.425	10.4	0.000370	0.11	59.896	0.738	0.0490	0.0011	0.0167	0.0002	106.6	1.3
14.1	551	331	0.602	8.2	-	0.52	58.039	0.747	0.0523	0.0013	0.0171	0.0002	109.6	1.4
Sample C5-R60B (location: S 76° 32.877, W 144° 41.248) ^{e,l}														
Rims														
3.1	137	64	0.47	1.8	-	1.06	65.652	0.985	0.0564	0.0018	0.0151	0.0002	96.4	1.5
4.1	124	74	0.60	1.6	0.000351	0.60	64.837	0.938	0.0527	0.0017	0.0153	0.0002	98.1	1.4
7.1	2615	515	0.20	123.3	0.000014	0.24	18.212	0.189	0.0553	0.0003	0.0548	0.0006	343.8	3.5

Table 1. (continued)

Grain Spot	U (ppm)	Th (ppm)	Th/U	²⁰⁶ Pb ^b (ppm)	²⁰⁴ Pb/ ²⁰⁶ Pb	f ₂₀₆ ^c (%)	Total ²³⁸ U/ ²⁰⁶ Pb	Error ^d	²⁰⁷ Pb/ ²⁰⁶ Pb	Error ^d	Radiogenic Ratios		Age (Ma)	
											²⁰⁶ Pb/ ²³⁸ U	Error ^d	²⁰⁶ Pb/ ²³⁸ U	Error ^d
9.1	449	41	0.09	5.8	0.000336	0.57	66.763	1.114	0.0525	0.0009	0.0149	0.0002	95.3	1.6
10.1	143	124	0.87	2.0	0.000310	0.78	60.418	0.914	0.0543	0.0017	0.0164	0.0003	105.0	1.6
11.1	766	345	0.45	10.4	0.000440	0.31	63.533	0.725	0.0505	0.0008	0.0157	0.0002	100.4	1.1
12.1	1379	682	0.49	18.9	0.000112	0.02	62.738	0.680	0.0482	0.0007	0.0159	0.0002	101.9	1.1
13.1	909	413	0.45	12.7	0.000133	0.20	61.662	0.805	0.0497	0.0007	0.0162	0.0002	103.5	1.3
14.1	933	23	0.03	12.7	0.000146	0.12	63.129	0.708	0.0490	0.0009	0.0158	0.0002	101.2	1.1
18.1	463	109	0.23	39.0	-	0.06	10.201	0.114	0.0605	0.0005	0.0980	0.0011	602.5	6.5
19.1	736	354	0.48	10.2	0.000189	0.03	62.256	0.737	0.0483	0.0008	0.0161	0.0002	102.7	1.2
21.1	1185	26	0.02	16.3	0.000116	0.05	62.380	0.690	0.0485	0.0006	0.0160	0.0002	102.5	1.1
Cores														
1.1	118	77	0.65	1.6	-	0.51	64.159	1.735	0.0520	0.0018	0.0155	0.0004	99.2	2.7
2.1	1710	1085	0.63	23.2	0.000051	0.34	63.175	0.765	0.0507	0.0004	0.0158	0.0002	100.9	1.2
5.1	1353	1094	0.81	19.1	-	0.43	60.912	0.797	0.0515	0.0005	0.0163	0.0002	104.5	1.4
6.1	58	39	0.68	0.8	0.003232	2.54	63.322	1.155	0.0681	0.0029	0.0154	0.0003	98.5	1.8
8.1	2720	3311	1.22	37.8	0.000017	0.38	61.793	0.646	0.0511	0.0004	0.0161	0.0002	103.1	1.1
15.1	605	430	0.71	8.4	0.000024	0.31	61.924	0.725	0.0505	0.0009	0.0161	0.0002	103.0	1.2
16.1	208	222	1.07	2.9	0.000296	0.46	61.495	0.858	0.0517	0.0017	0.0162	0.0002	103.5	1.5
17.1	569	421	0.74	27.2	0.000031	0.17	17.965	0.197	0.0548	0.0005	0.0556	0.0006	348.6	3.8
20.1	114	78	0.69	1.6	0.002421	1.02	59.392	0.992	0.0563	0.0023	0.0167	0.0003	106.5	1.8
22.1	939	542	0.58	12.8	0.000006	<0.01	62.908	0.724	0.0476	0.0007	0.0159	0.0002	101.7	1.2
Sample M5-G174 (location: S 76° 33.237, W 145° 12.055) ^{e,m}														
Rims														
1.1	125	39	0.31	14.6	0.000013	0.86	7.338	0.390	0.0734	0.0019	0.1351	0.0074	816.9	42.1
3.1	331	93	0.28	26.4	0.000075	<0.01	10.760	0.137	0.0585	0.0004	0.0930	0.0012	573.3	7.1
4.1	936	55	0.06	51.6	0.000039	0.06	15.592	0.186	0.0552	0.0006	0.0641	0.0008	400.5	4.7
5.1	420	223	0.53	36.3	0.000080	0.09	9.946	0.107	0.0611	0.0004	0.1004	0.0011	617.0	6.5
8.1	387	328	0.85	19.7	0.000153	0.29	16.907	0.187	0.0563	0.0006	0.0590	0.0007	369.4	4.0
9.1	72	100	1.38	0.9	0.000680	1.34	66.255	1.148	0.0586	0.0026	0.0149	0.0003	95.3	1.7
12.1	577	256	0.44	26.9	0.000092	0.11	18.435	0.200	0.0542	0.0005	0.0542	0.0006	340.2	3.6
14.1	353	80	0.23	26.6	0.000059	<0.01	11.389	0.354	0.0581	0.0005	0.0878	0.0028	542.7	16.5
15.1	1334	253	0.19	19.2	0.000105	0.11	59.645	0.661	0.0490	0.0006	0.0167	0.0002	107.1	1.2
26.1	399	576	1.44	5.4	0.000036	0.63	63.395	0.796	0.0530	0.0012	0.0157	0.0002	100.3	1.3
Cores														
2.1	608	111	0.18	53.0	-	0.02	9.862	0.115	0.0607	0.0004	0.1014	0.0012	622.4	7.0
6.1	538	209	0.39	7.3	0.000239	0.08	63.425	0.731	0.0486	0.0009	0.0158	0.0002	100.8	1.2
7.1	1365	68	0.05	19.5	0.000074	<0.01	60.269	0.725	0.0481	0.0006	0.0166	0.0002	106.1	1.3
10.1	114	98	0.85	1.7	0.000199	1.11	58.299	0.912	0.0570	0.0047	0.0170	0.0003	108.4	1.8
11.1	477	396	0.83	49.6	0.000091	0.64	8.257	0.089	0.0690	0.0007	0.1203	0.0013	732.4	7.7
13.1	563	185	0.33	80.3	0.000033	<0.01	6.023	0.064	0.0714	0.0003	0.1662	0.0019	991.0	10.2
16.1	454	1226	2.70	6.2	0.000751	1.15	62.863	0.745	0.0571	0.0010	0.0157	0.0002	100.6	1.2
17.1	247	29	0.12	41.5	0.000045	0.10	5.111	0.057	0.0790	0.0005	0.1955	0.0023	1150.9	12.3
18.1	64	67	1.05	0.8	0.002715	4.01	64.857	1.261	0.0797	0.0035	0.0148	0.0003	94.7	1.9
19.1	301	117	0.39	26.9	0.000131	1.30	9.621	0.109	0.0714	0.0006	0.1026	0.0012	629.6	7.0
22.1	474	86	0.18	22.3	0.000160	0.05	18.220	0.208	0.0538	0.0006	0.0549	0.0006	344.3	3.9
23.1	346	195	0.56	23.9	0.000109	<0.01	12.450	0.141	0.0570	0.0006	0.0803	0.0009	498.1	5.5
24.1	265	465	1.75	3.6	0.002798	5.21	62.546	0.843	0.0893	0.0052	0.0152	0.0002	97.0	1.5
25.1	174	134	0.77	2.3	0.001514	1.38	66.099	1.011	0.0589	0.0020	0.0149	0.0002	95.5	1.5
27.1	181	244	1.35	2.4	0.002606	2.06	64.288	0.963	0.0644	0.0036	0.0152	0.0002	97.5	1.5

^aDatum = WGS84.^bCorrection for common Pb made using the measured ²³⁸U/²⁰⁶Pb and ²⁰⁷Pb/²⁰⁶Pb ratios following *Tera and Wasserburg* [1972] as outlined by *Williams* [1998].^cHere f₂₀₆ (%) denotes the percentage of ²⁰⁶Pb that is common Pb.^dUncertainties given at the 1σ level.^eError in Temora reference zircon calibration was 0.29% for the analytical session (not included in above errors but required when comparing data from different mounts).^fGranite sheet from southern Mount Iphigene.^gError in Temora reference zircon calibration was 0.39% for the analytical session (not included in above errors but required when comparing data from different mounts).^hGranitic sill from within the diatexite migmatite unit at Mount Ferranto.ⁱGranodioritic sigmoidal boudin from Mount Richardson.^jConcordant granite from Mount Richardson.^kGranite in discordant shear band Mount Richardson.^lSyntectonic granite sheet from Mount Richardson.^mGranitic dike from Mount Getz.

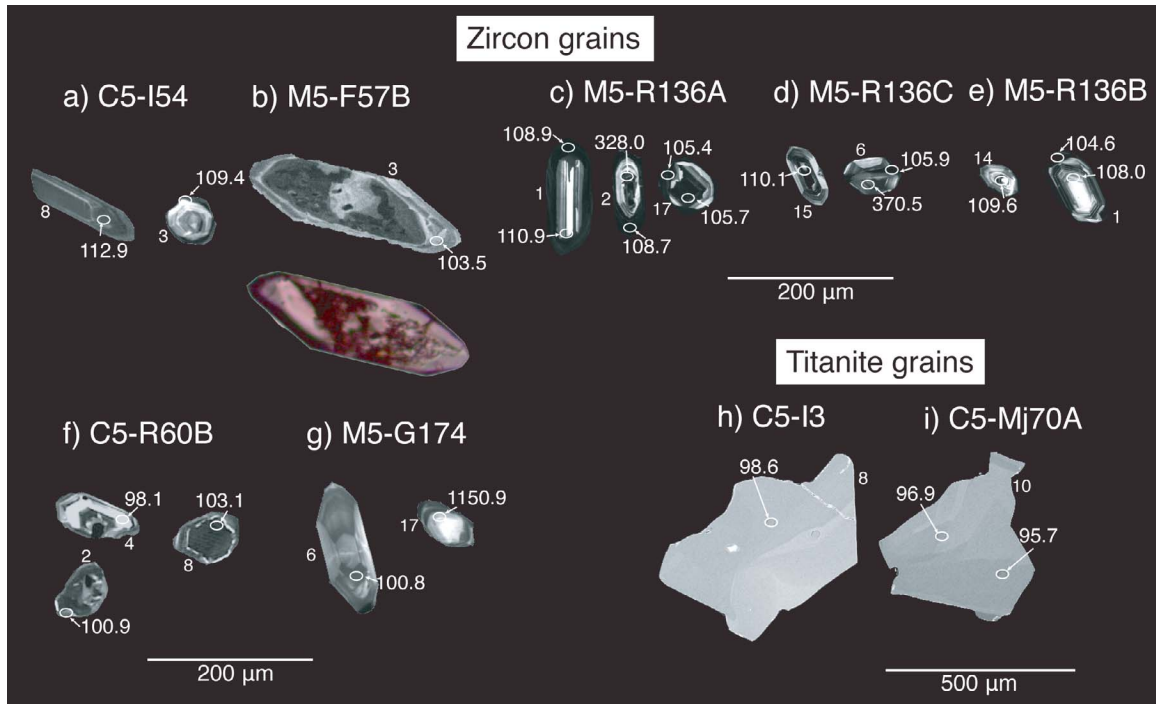


Figure 7. CL and BSE images of selected grain types and areas analyzed for SHRIMP U-Pb geochronology. Small numbers refer to grain number designations in Table 1. Large numbers are $^{206}\text{Pb}/^{238}\text{U}$ ages in Ma for individual area analyses (see Table 1 for corresponding error on area analyses).

The U/Pb ratios for titanite have been normalized relative to a value of 0.17636 for the BLR-1 titanite standard, from a Namibian pegmatite (1047 Ma) [Aleinikoff *et al.*, 2007].

[32] Uncertainties given for individual analyses (ratios and ages) are at the one-sigma level (Table 1). Tera-Wasserburg [Tera and Wasserburg, 1972] concordia plots, probability density plots with stacked histograms, and weighted mean $^{206}\text{Pb}/^{238}\text{U}$ age calculations were carried out using ISOPLOT/EX [Ludwig, 2003]. The “Mixture Modeling” algorithm of Sambridge and Compston [1994], via ISOPLOT/EX, was used to un-mix statistical age populations or groupings. These groupings were used to calculate weighted mean $^{206}\text{Pb}/^{238}\text{U}$ ages and the uncertainties are reported as 95% confidence limits. We analyzed distinct rim and core domains of the zircon grains based on the CL images (Figure 7).

[33] Analyses of rare earth element (REE) and trace element concentrations for zircons of known age were conducted to acquire geochemical information on zircon formation processes and source materials [e.g., Ireland and Wlotzka, 1992; Maas *et al.*, 1992]. REE data were acquired using SHRIMP RG at The Australian National University-Research School of Earth Sciences for selected spots that had been analyzed for U-Pb geochronology. The energy filtering method was used to reduce interferences [Ireland and Wlotzka, 1992; Guo *et al.*, 1996] and in most instances two isotopes were measured (Table 2) so that the isotopic ratios could be used to check for isobaric interferences. Operating conditions and data reduction methods are as in the work of Hoskin [1998]. REE detection limits are in the vicinity of 0.01 ppm for the analysis spots that are 30 μm across and a few μm deep.

Table 2. REE and Trace Element Data for Two Cretaceous Zircons^a

Area	La	Ce	Pr	Nd	Sm	Eu	Gd	Tb	Dy	Ho	Er	Tm	Yb	Lu	Hf	Y
1.1	0.005	14.60	0.029	0.53	2.92	0.54	28.71	16.90	244.4	104.0	520.9	126.3	1302.4	259.3	19009	3579.4
1.1				0.78	3.02	0.50	28.81		246.4		511.2		1312.8		19067	
1.2	0.008	52.69	0.190	3.22	7.54	1.95	37.53	15.03	175.6	68.3	318.3	71.1	692.3	140.1	14111	2221.098
1.2				3.20	7.56	1.95	38.07		178.4		308.2		704.1		14207	
17.1	0.002	6.60	0.016	0.22	1.33	0.31	11.54	6.70	101.3	46.2	252.7	72.2	849.8	192.9	18125	1462.182
17.1				0.24	1.33	0.32	11.16		104.2		247.7		865.7		18174	
17.2	3.346	456.45	2.674	15.16	12.94	2.51	65.60	30.14	403.6	174.2	875.0	202.8	1975.5	384.0	16189	6552.751
17.2				14.49	13.30	2.32	64.96		406.6		865.2		1993.8		16336	

^aZircons are from sample M5-R136A and were analyzed on the SHRIMP RG. All REE and Y concentrations are in ppm. Analyses were conducted against standard glass. Zircon, isotope $\mu\text{mol/g}$ = 153.187; Zircon isotope ppm = 13940.

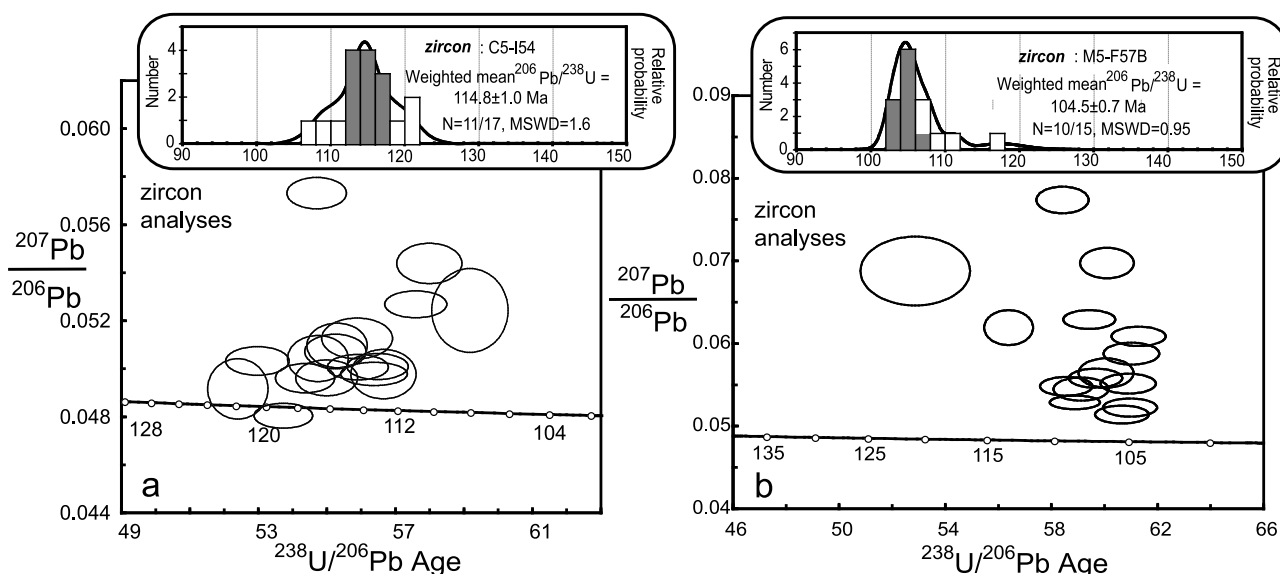


Figure 8. Tera-Wasserburg concordia diagrams of SHRIMP U-Pb isotopic data. Analyses are plotted as 1- σ error ellipses. Insets are probability density plots with stacked histograms calculated using ISOPLOT [Ludwig, 2003]. Analyses used to calculate the weighted mean age are gray. Analyses that were more than 2- σ from the mean are white and were not used to determine the weighted mean age. Weighted mean $^{206}\text{Pb}/^{238}\text{U}$ age and uncertainty is given at 95% confidence and includes the uncertainty in the U/Pb ratio calibration of the reference zircon. (a) Recumbently folded granite sheet, C5-I54, from within the orthogneiss complex and (b) 20 cm-thick granite sill, M5-F57B, from within the diatexite migmatite unit.

5.2. Zircon and Titanite Morphology and Geochronology

[34] The Fosdick Mountains preserve evidence for two major anatectic events, one during Devonian-Carboniferous time and one during Jurassic-Cretaceous time [Siddoway *et al.*, 2004b; Siddoway and Fanning, 2009; Korhonen *et al.*, 2010a]. Inherited grains reflect this polyphase history. This study focuses on the Jurassic-Cretaceous event and uses U-Pb geochronology to document magma crystallization and emplacement during oblique extension in a migmatite-cored gneiss dome.

5.2.1. Characterization of Zircon From Steep Domains

[35] Zircon populations from the folded biotite granite sheet (C5-I54) from within the orthogneiss complex are 1) euhedral to subhedral, acicular to more equant proportioned bipyramidal grains and 2) round grains (Figure 7a). Euhedral grains form the majority of the C5-I54 mineral separate. The euhedral grains display weak oscillatory zoning with low U (bright in CL) cores and wide, high U (dark in CL) rims or tips. Crystals are typically 100–250 μm in length with an axial ratio of 2:1. Euhedral grain rims have high U, low Th concentrations, and low Th/U ratios. Round grains are less abundant. Their round or oval shape suggests that they originated as inherited grains. The round grains have slightly irregular margins and occasionally wide, high U rims. The grains have cores with low U, low Th concentrations, and moderate Th/U ratios and rims with high U, low Th concentrations, and very low Th/U ratios.

[36] Rim and core analyses of the Cretaceous zircon grains give ages between ca. 121 and 107 Ma. Some zircon

grains, interpreted to be inherited, give Devonian to Proterozoic ages. Eleven analyses from the Cretaceous population yield a weighted mean $^{206}\text{Pb}/^{238}\text{U}$ age of 114.8 ± 1.1 Ma (N = 11/17: used/total) (Figure 8a; Table 1).

[37] The folded, steeply dipping leucogranite sill (M6-L188) from within the leucogranite sheeted complex at Mount Lockhart has a weighted mean $^{206}\text{Pb}/^{238}\text{U}$ age of 116.3 ± 1.0 Ma [McFadden *et al.*, 2010]. Korhonen *et al.* [2010b], using LA-ICP-MS, analyzed zircons from a granite emplaced in steep foliation (K6-Mt38) from Mutel Peak and determined a weighted mean $^{206}\text{Pb}/^{238}\text{U}$ age of 114 ± 5 Ma.

5.2.2. Characterization of Zircon From Subhorizontal Domains and the South Fosdick Detachment Zone

[38] Zircon populations from the 20 cm-thick concordant granite sill (M5-F57B) from within the diatexite migmatite unit are predominantly prismatic bipyramidal grains, 100–300 μm in size, with oscillatory-zoned, moderate U overgrowths surrounding high U, corroded cores (Figure 7b). Rims have high U, low Th concentrations, and very low Th/U ratios. Rim ages are between ca. 111 and 102 Ma, with a prevalence of younger grains that yielded a weighted mean $^{206}\text{Pb}/^{238}\text{U}$ age of 104.5 ± 0.8 Ma (N = 10/15) (Figure 8b; Table 1).

[39] The subhorizontal leucogranite sheet (C6-BB112) from within the leucogranite sheeted complex at Bird Bluff has a weighted mean $^{206}\text{Pb}/^{238}\text{U}$ age of 103.6 ± 0.7 Ma [McFadden *et al.*, 2010]. Another subhorizontal granite sheet (K6-Bb47) sampled from within the leucogranite sheeted complex at Bird Bluff has a weighted mean $^{206}\text{Pb}/^{238}\text{U}$ age of 109 ± 2 Ma and a garnet-bearing 1 m-

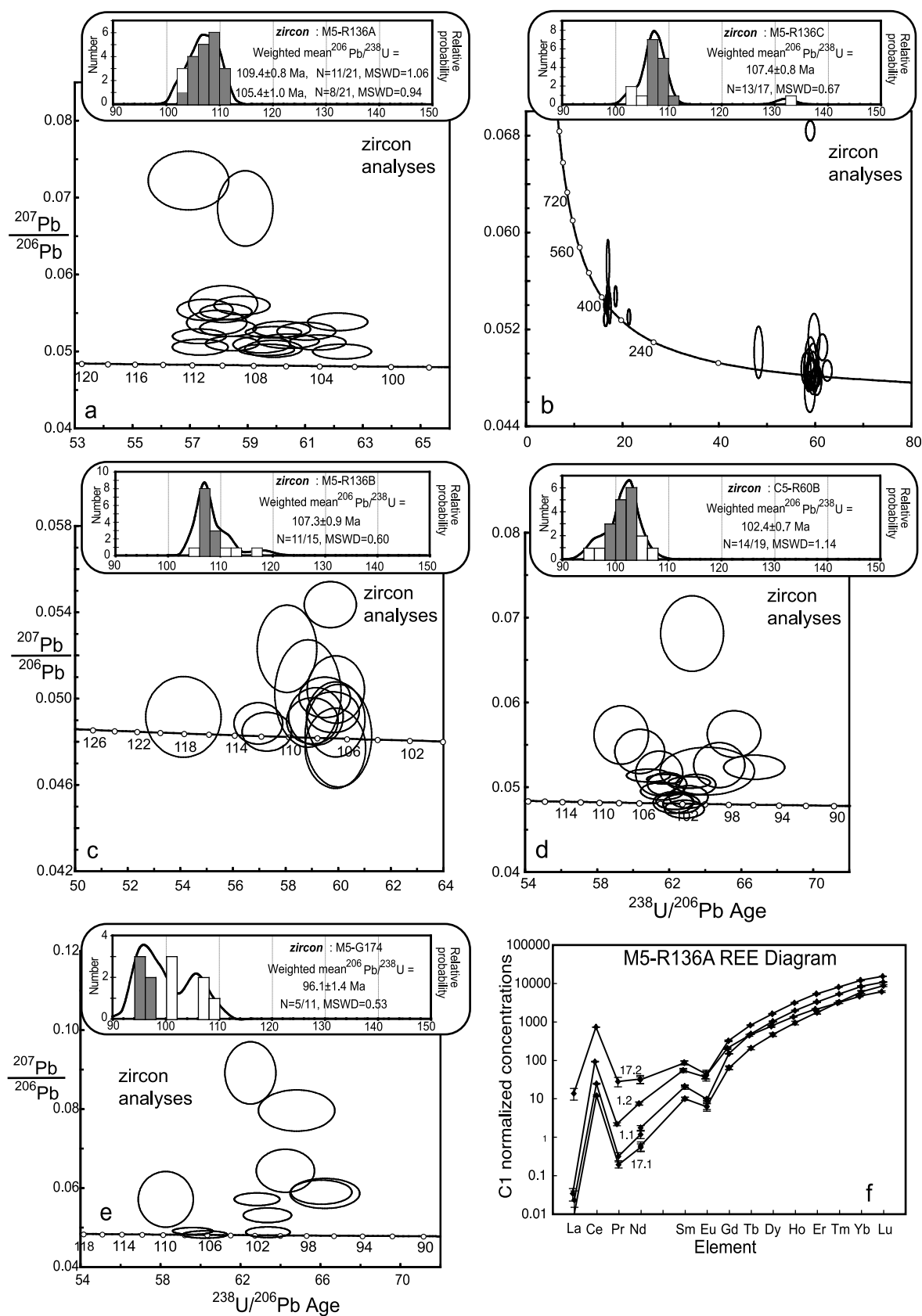


Figure 9

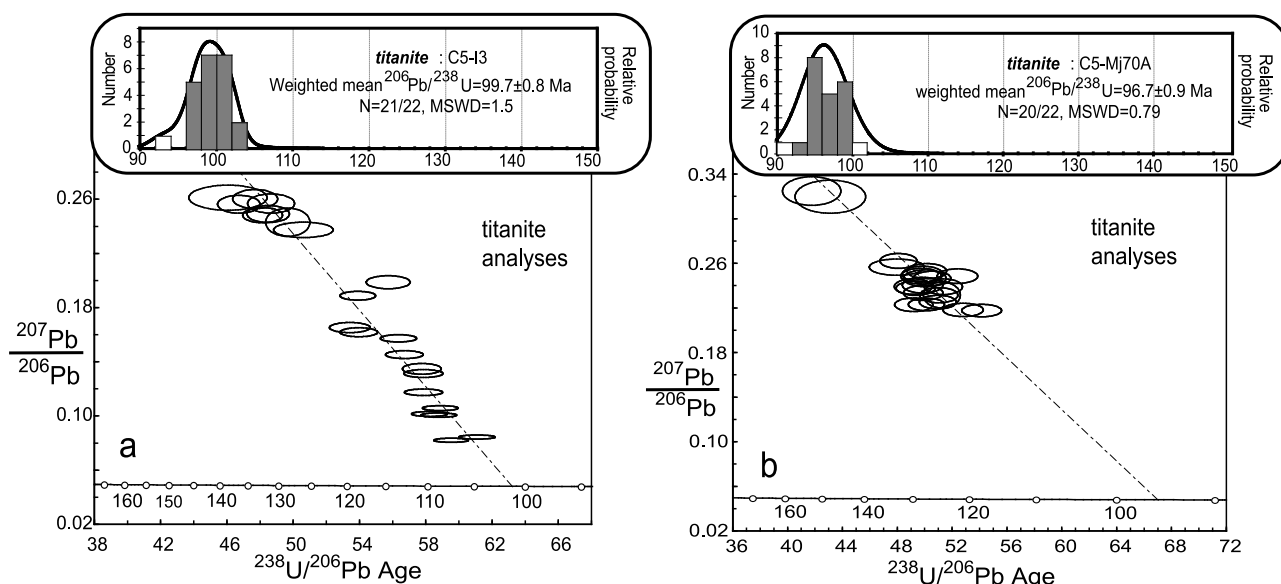


Figure 10. Tera-Wasserburg concordia diagram of isotopic data from SHRIMP-RG for diorite dikes (a) C5-I3 and (b) C5-Mj70A. Analyses plotted as 1- σ error ellipses. The three-dimensional linear regression line is shown from the measured $^{207}\text{Pb}/^{206}\text{Pb}$ ratio for each analysis along with total $^{207}\text{Pb}/^{206}\text{Pb}$ and $^{238}\text{U}/^{206}\text{Pb}$ ratios to define a lower concordia intercept. Insets are probability density plots with stacked histograms calculated using ISOPLOT [Ludwig, 2003]. Analyses used to calculate the weighted mean age are gray. Analyses that were more than 2- σ from the mean are white and were not used to determine the weighted mean age.

thick granite sill (K6-Mj01) from the diatexite migmatite unit at Marujupu Peak has a weighted mean $^{206}\text{Pb}/^{238}\text{U}$ age of 102 ± 3 Ma [Korhonen *et al.*, 2010b].

[40] Zircon populations for the boudinaged granodioritic orthogneiss (M5-R136A) are 1) prismatic and acicular grains with bipyramidal terminations, and 2) round grains. The euhedral grains are 100–400 μm in length with a 2:1 to 3:1 axial ratio (Figure 7c). Under CL, the grains display oscillatory-zoned core domains, embayments, and corroded textures, with wide, high U rims. Rims have high U, low Th concentrations, and low Th/U ratios, whereas cores have moderate U, low Th concentrations, and moderate Th/U ratios. The round grains are ~ 100 μm with high U cores and moderate U rims. Cores have moderate Th/U ratios and rims have low Th/U ratios.

[41] Core analyses fall in two distinct age groups: Devonian-Carboniferous ages in the range ca. 368 to 357 Ma, and Cretaceous ages in the range ca. 111 to 105 Ma. The rims give Cretaceous ages in the range ca. 110 to 102 Ma. The zircon rim analyses show a broad bimodal age distribution with a tail at the young side that may be a consequence of Pb loss. The older sub-maxima yielded a weighted mean $^{206}\text{Pb}/^{238}\text{U}$ age of 109.1 ± 0.8 Ma ($N = 11/21$) and the younger sub-maxima yielded a weighted mean $^{206}\text{Pb}/^{238}\text{U}$ age of 105.4 ± 1.0 Ma ($N = 8/21$) (Figure 9a; Table 1).

[42] The concordant biotite granite (M5-R136C) contains zircon grains quite similar to M5-R136A in morphology and luminescence (Figure 7d). The grains are a mixed population of euhedral to subhedral grains that are acicular or prismatic with bipyramidal terminations. Under CL, grains

Figure 9. Tera-Wasserburg concordia diagrams of SHRIMP U-Pb isotopic data. Analyses are plotted as 1- σ error ellipses. Insets are probability density plots with stacked histograms calculated using ISOPLOT [Ludwig, 2003]. Analyses used to calculate the weighted mean age are gray. Analyses that were more than 2- σ from the mean are white and were not used to determine the weighted mean age. Weighted mean $^{206}\text{Pb}/^{238}\text{U}$ age and uncertainty is given at 95% confidence and includes the uncertainty in the U/Pb ratio calibration of the reference zircon. (a) Boudinaged granodioritic orthogneiss, sample M5-R136A, (b) concordant granite sill, sample M5-R136C, (c) granite-filled shear band, sample M5-R136B, and (d) syntectonic tabular granite sheet, sample C5-R60B, and (e) granitic dike, sample M5-G174. f) Rare earth element (REE) data from the core and rim of two igneous grains from two zircon populations in sample M5-R136A from the Mount Richardson. Data are provided in Table 2. Plot is normalized to chondrite. Grain 1 is from the dominant zircon population of prismatic grains and grain 17 is from the less common population of round grains. Both core and rim analyses record Cretaceous ages. Core and rim analyses for both grains have steeply rising slopes from light REE to heavy REE, with positive Ce and negative Eu anomalies. However, the rim analysis from grain 17 (17.2) has a significantly higher concentration of La and Ce, creating a shallower slope from light REE to heavy REE.

Table 3. Summary of SHRIMP U-Pb Titanite Results for Diorite Dikes in the Fosdick Mountains^a

Grain Spot	U (ppm)	Th (ppm)	Th/U	²⁰⁶ Pb ^b	²⁰⁴ Pb/ ²⁰⁶ Pb	Error ^c	f_{206}^d	Total ²³⁸ U/ ²⁰⁶ Pb	Error ^c	²⁰⁷ Pb/ ²⁰⁶ Pb	Error ^c	Radiogenic Ratios		Age (Ma)	
				(ppm)			(%)					²⁰⁶ Pb/ ²³⁸ U	Error ^c	²⁰⁶ Pb/ ²³⁸ U	Error ^c
Sample C5-I3 (location: S 76° 32.318, W 145° 51.061) ^{e,f}															
Fraction B															
1.1	92	232	2.53	1.7	0.010115	0.001480	26.92	46.160	1.546	0.2619	0.0061	0.0158	0.0006	101.3	3.6
1.2	63	160	2.55	1.1	0.015902	0.001605	26.32	46.800	0.840	0.2571	0.0043	0.0157	0.0003	100.7	2.1
1.3	56	125	2.24	1.0	0.012680	0.001896	26.39	48.738	0.924	0.2576	0.0046	0.0151	0.0003	96.6	2.1
2.1	311	397	1.28	4.6	0.003421	0.000399	7.04	58.255	0.710	0.1040	0.0012	0.0160	0.0002	102.1	1.3
3.1	73	186	2.55	1.2	0.012256	0.001282	23.96	50.668	1.178	0.2382	0.0038	0.0150	0.0004	96.0	2.4
4.1	446	546	1.22	6.4	0.002962	0.000280	4.63	59.558	0.689	0.0848	0.0009	0.0160	0.0002	102.4	1.2
5.1	104	119	1.14	1.6	0.010274	0.001086	19.19	55.751	0.871	0.2003	0.0031	0.0145	0.0002	92.8	1.6
6.1	65	88	1.35	1.1	0.012395	0.001435	24.66	49.731	0.879	0.2438	0.0068	0.0151	0.0003	96.9	2.1
Fraction A															
1.1	122	131	1.08	2.0	0.007110	0.000847	15.00	53.469	0.796	0.1672	0.0025	0.0159	0.0003	101.7	1.6
1.2	415	311	0.75	5.8	0.002336	0.000275	4.94	61.100	0.711	0.0873	0.0010	0.0156	0.0002	99.5	1.2
2.1	151	790	5.23	2.4	0.006855	0.000732	14.55	54.005	0.751	0.1636	0.0022	0.0158	0.0002	101.2	1.5
2.2	55	229	4.15	1.0	0.013969	0.001574	26.79	47.764	0.890	0.2607	0.0045	0.0153	0.0003	98.1	2.1
3.1	206	209	1.02	3.1	0.005856	0.000562	9.06	57.890	0.753	0.1200	0.0016	0.0157	0.0002	100.5	1.3
4.1	66	243	3.65	1.2	0.010832	0.001246	25.44	48.564	0.845	0.2500	0.0040	0.0154	0.0003	98.2	1.9
5.1	196	202	1.03	3.0	0.006786	0.000613	12.52	56.726	0.742	0.1474	0.0018	0.0154	0.0002	98.7	1.3
6.1	332	401	1.21	4.8	0.003916	0.000380	7.57	58.890	0.704	0.1081	0.0012	0.0157	0.0002	100.4	1.2
6.2	331	342	1.03	4.8	0.003676	0.000372	6.95	58.804	0.703	0.1032	0.0012	0.0158	0.0002	101.2	1.2
7.1	78	310	4.00	1.4	0.013814	0.001301	25.30	48.219	0.787	0.2490	0.0037	0.0155	0.0003	99.1	1.8
8.1	178	193	1.08	2.6	0.005828	0.001109	10.76	57.887	0.773	0.1335	0.0018	0.0154	0.0002	98.6	1.4
9.1	188	235	1.25	3.0	0.008623	0.000702	17.92	53.944	0.708	0.1903	0.0021	0.0152	0.0002	97.3	1.4
10.1	226	250	1.10	3.4	0.007496	0.000606	13.99	56.389	0.716	0.1591	0.0018	0.0153	0.0002	97.6	1.3
11.1	187	233	1.25	2.8	0.006104	0.000624	11.21	57.796	0.763	0.1370	0.0025	0.0154	0.0002	98.3	1.4
Sample C5-Mj70A (location: S 76° 31.101 W 145° 39.023) ^{e,g}															
1.1	60	522	8.67	1.0	0.014508	0.001804	25.34	52.483	0.969	0.2490	0.0045	0.0142	0.0003	91.1	1.9
2.1	72	283	3.93	1.1	0.012198	0.001377	21.46	54.242	0.937	0.2183	0.0038	0.0145	0.0003	92.7	1.8
3.1	65	458	7.10	1.1	0.011924	0.001372	22.40	51.064	0.900	0.2259	0.0039	0.0152	0.0003	97.2	1.9
4.1	21	35	1.64	0.4	0.023623	0.003149	34.34	43.163	1.704	0.3208	0.0098	0.0152	0.0007	97.3	4.3
5.1	53	331	6.27	0.9	0.015509	0.001730	25.32	49.803	0.984	0.2490	0.0048	0.0150	0.0003	95.9	2.1
6.1	54	340	6.31	0.9	0.012187	0.001540	24.34	49.914	0.975	0.2413	0.0046	0.0152	0.0003	97.0	2.1
7.1	66	307	4.64	1.2	0.010344	0.001362	22.07	49.304	0.906	0.2234	0.0042	0.0158	0.0003	101.1	2.0
8.1	58	316	5.41	1.0	0.012975	0.002037	23.43	49.983	0.962	0.2341	0.0044	0.0153	0.0003	98.0	2.1
8.2	58	336	5.80	1.2	0.020179	0.002912	34.99	41.864	1.413	0.3260	0.0086	0.0155	0.0006	99.3	3.9
9.1	53	332	6.27	0.9	0.015226	0.001742	26.38	48.042	1.327	0.2575	0.0048	0.0153	0.0005	98.0	2.9
10.1	49	262	5.30	0.8	0.013975	0.001823	25.12	50.089	1.013	0.2474	0.0049	0.0149	0.0003	95.7	2.2
10.2	59	402	6.81	1.1	0.015007	0.001634	27.06	48.181	0.888	0.2629	0.0045	0.0151	0.0003	96.9	2.0
11.1	52	313	6.06	0.9	0.015843	0.002194	25.59	49.929	0.981	0.2511	0.0048	0.0149	0.0003	95.4	2.1
12.1	63	348	5.50	1.1	0.012198	0.001377	24.12	51.448	0.929	0.2395	0.0047	0.0147	0.0003	94.4	1.9
13.1	66	527	7.94	1.1	0.010734	0.001262	23.19	51.135	0.921	0.2321	0.0045	0.0150	0.0003	96.1	1.9
14.1	62	499	8.09	1.0	0.011252	0.001349	21.54	52.897	0.969	0.2189	0.0040	0.0148	0.0003	94.9	1.9
15.1	72	556	7.74	1.2	0.011216	0.001265	22.12	50.240	0.857	0.2237	0.0037	0.0155	0.0003	99.2	1.9
15.2	57	431	7.53	1.0	0.014383	0.001548	25.13	50.640	0.920	0.2474	0.0043	0.0148	0.0003	94.6	1.9
15.3	66	556	8.36	1.1	0.012536	0.001386	23.21	51.356	0.895	0.2323	0.0078	0.0150	0.0003	95.7	2.1
16.1	56	353	6.34	1.0	0.012957	0.001565	24.16	49.254	0.925	0.2399	0.0044	0.0154	0.0003	98.5	2.1
16.2	58	370	6.34	1.0	0.014447	0.001684	23.99	49.421	0.920	0.2385	0.0043	0.0154	0.0003	98.4	2.0
17.1	53	303	5.70	0.9	0.014188	0.001563	25.90	50.258	0.944	0.2536	0.0046	0.0147	0.0003	94.4	2.0

^aDatum = WGS84.^bCorrection for common Pb made using the measured ²³⁸U/²⁰⁶Pb and ²⁰⁷Pb/²⁰⁶Pb ratios following *Tera and Wasserburg* [1972] as outlined by *Williams* [1998].^cUncertainties given at the 1σ level.^df₂₀₆ % denotes the percentage of ²⁰⁶Pb that is common Pb.^eError in BLR-1 reference titanite calibration was 0.43% for the analytical session (not included in above errors but required when comparing data from different mounts).^fDiorite dike from southern Mount Iphigene.^gDiorite dike from central Marujupu.

have oscillatory-zoned core domains, embayments, and high U rims. Rims are commonly homogeneous. Rims predominantly have high U, low Th concentrations, and low Th/U ratios, whereas cores commonly have moderate U, moderate Th concentrations, and moderate to high Th/U ratios. Core and rim analyses reveal a Devonian-Carboniferous group in

the range ca. 379 to 358 Ma, interpreted to be inherited grains, and a Cretaceous group in the range ca. 110 to 102 Ma. The Cretaceous analyses yielded a weighted mean ²⁰⁶Pb/²³⁸U age of 107.4 ± 0.8 Ma (N = 13/17) (Figure 9b; Table 1).

[43] Zircon grains from the discordant granite-filled shear band (M5-R136B) are predominantly pristine, prismatic

grains with bipyramidal terminations (Figure 7e), oscillatory-zoned cores, and high U rims. Rims have high U, low Th concentrations with very low Th/U ratios. The cores of the prismatic grains have moderate to low U, moderate to high Th concentrations, and high Th/U ratios. Analyses of rim and cores give Cretaceous ages in the range ca. 118 to 104 Ma. No zircons gave Devonian-Carboniferous ages, however one grain recorded a Proterozoic age. The Cretaceous rims and cores yielded a weighted mean $^{206}\text{Pb}/^{238}\text{U}$ age of 107.3 ± 0.9 Ma ($N = 11/15$) (Figures 9c; Table 1).

[44] Zircon populations from the tabular leucogranite sheet (C5-R60B) include: 1) blocky, bipyramidal, oscillatory-zoned grains that are 100–400 μm in length and 2) round grains with cores of uniform brightness in CL (Figure 7f). Blocky prismatic zircons are the most common type and they display a wide, low U rim succeeded by a narrow high U rim overgrowth upon low U, euhedral cores or moderate U, round cores. Blocky zircon rims have moderate Th/U ratios and cores have high Th/U ratios. Round zircons are small with uniform moderate to low U cores. Round grain rims have low Th/U ratios and cores have high Th/U ratios.

[45] Rim and core analyses yield two Carboniferous ages that are interpreted to be inherited grains and Cretaceous ages in the range ca. 106 to 95 Ma. The Cretaceous analyses yielded a weighted mean $^{206}\text{Pb}/^{238}\text{U}$ age of 102.4 ± 0.7 Ma ($N = 14/19$) (Figure 9d; Table 1).

[46] Zircon populations from the two-mica granite dike (M5-G174) that crosscuts the gneissic foliation in the South Fosdick Detachment zone at Mount Getz include: 1) blocky and acicular, euhedral grains, 100–250 μm in length and 2) small, round grains 50–150 μm in length (Figure 7g). Euhedral grains have oscillatory-zoned low U cores with high U rims. Round grains have oscillatory-zoned, inherited cores that range from low to high U, overgrown by oscillatory-zoned rims that embay the inherited cores.

[47] Older age groups have a wide scatter of Neoproterozoic and Paleozoic ages. Eleven analyses fall in the range 107 to 95 Ma, with no systematic difference between core and rim results. The best estimate for a weighted mean $^{206}\text{Pb}/^{238}\text{U}$ age for this sample is 96.1 ± 1.4 Ma ($N = 5/11$) (Figure 9e; Table 1). Unfortunately, these data are not robust enough to make any further geologic interpretations, so this sample will not be discussed any further.

5.2.3. Rare Earth Element Data for Sample M5-R136A

[48] Rare earth element data (REE) was collected from two igneous zircons in sample M5-R136A (Table 2). The data were normalized to chondrite (Figure 9f). Core and rim analyses show similar patterns with steeply rising slopes from light REE to heavy REE. They also both show positive Ce and negative Eu anomalies. The values are consistent with typical crustal zircons [Hoskin and Schaltegger, 2003].

5.2.4. Late- to Post-Tectonic Dikes

[49] Two late to post-tectonic diorite dikes that do not contain zircon were dated using titanite U-Pb geochronology. Titanite grains from both dikes are red-brown, clear, and sub- to euhedral. In BSE images, the grains display oscillatory growth zoning and less common sector zoning

(Figures 7h and 7i). Some grains display high U (bright in BSE) embayments. The analyzed mineral separates are grain fragments that were broken during hand crushing and picking. Titanite crystals are 2 to 6 mm in size in sample C5-I3, the folded and interdigitated diorite dike from southern Mount Iphigene, and 0.3 to 1 mm in sample C5-Mj70A, the tabular, discordant diorite dike on Marujupu Peak. C5-I3 analyses have higher U and lower Th concentrations than C5-Mj70A, with C5-Mj70A having a higher Th/U ratio.

[50] The folded dike from southern Mount Iphigene (C5-I3) gave Cretaceous $^{206}\text{Pb}/^{238}\text{U}$ titanite ages in the range ca. 102 to 94 Ma for center and edge analyses. The analyses define a simple distribution with a weighted mean $^{206}\text{Pb}/^{238}\text{U}$ age of 99.7 ± 0.9 Ma ($N = 21/22$) (Figure 10a; Table 3). One analysis that is younger is considered to have lost radiogenic Pb. The three-dimensional linear fit shows evidence of significant common Pb, giving an age of 101.2 ± 1.2 Ma. The $^{206}\text{Pb}/^{238}\text{U}$ ages for the tabular, discordant dike from Marujupu Peak are in the range ca. 101 to 94 Ma. The weighted mean $^{206}\text{Pb}/^{238}\text{U}$ age is 96.7 ± 1.0 Ma ($N = 20/22$) (Figure 10b; Table 3). The grains are enriched in common Pb and cluster so that the linear three-dimensional fit is not an effective way of treating the data set.

6. Discussion

6.1. Controls on Fabric Development and Magma Emplacement

[51] Structural observations from western Marie Byrd Land and the Fosdick Mountains indicate that the region experienced transcurrent deformation that affected the brittle upper crust and the ductile middle to lower crust [Siddoway *et al.*, 2004b, 2005; McFadden *et al.*, 2007]. The quality of exposure in the Fosdick dome, together with structural and geochronological work, allows us to evaluate the interrelationships among transcurrent deformation, fabric development, and magma emplacement.

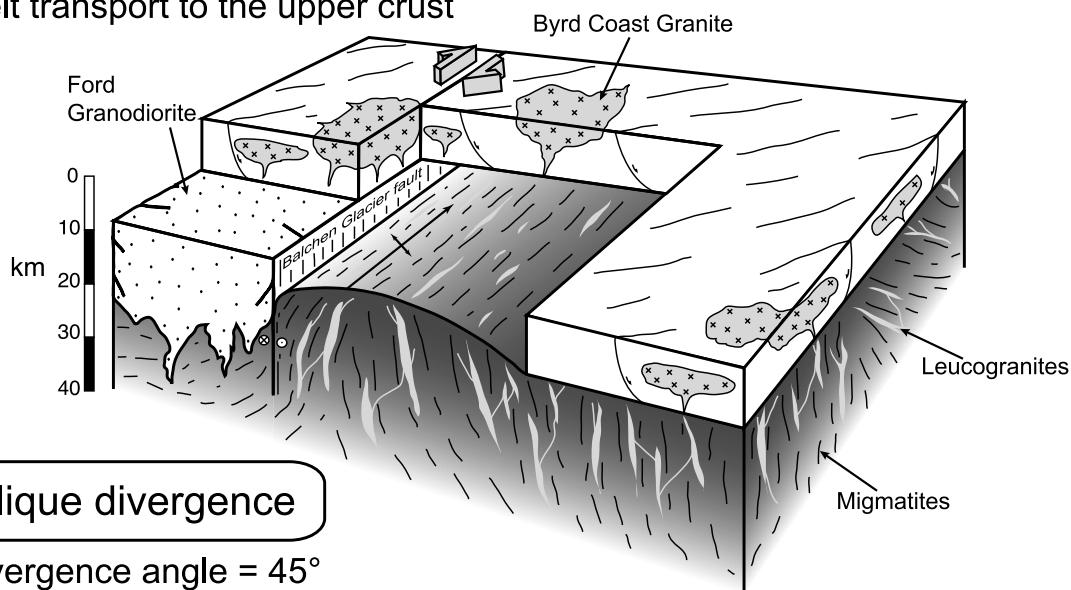
[52] Transensional strain theory [e.g., Teyssier and Tikoff, 1999] provides a framework in which to understand the geometries of fabrics preserved in the Fosdick dome, where early steep foliations with scarce lineation are overprinted by subhorizontal foliation with well-developed lineation [McFadden *et al.*, 2010] (Figures 5f–5h). The steep structures generally align with the regional finite strain axes oriented 075° – 265° [Siddoway *et al.*, 2005]. We infer the steep foliations developed during wrench deformation. The steep structures are strongly overprinted by subhorizontal foliations and recumbent folds that trend 055° – 235° . Thus, the foliations, lineations, and fold hinge lines of the dome and the long axis of the dome provide a record of a rotation of strain axes from ENE-directed wrench to NE–SW oblique extension [McFadden *et al.*, 2010] (Figure 11a).

[53] The subhorizontal foliation domains have stretching lineations that trend 055° – 235° (Figure 4) and nappe-scale and dm- to m-scale recumbent fold hinge lines have similar trends of 060° – 240° that suggest contemporaneity of mesoscopic and megascopic folds. We interpret the dominant trend of $235^\circ \pm 5^\circ$ from lineations and fold hinge lines

a)

Wrench deformation

- Divergence angle = 0°
- Melt transport to the upper crust



b)

Oblique divergence

- Divergence angle = 45°
- Magma accumulation in the Fosdick dome

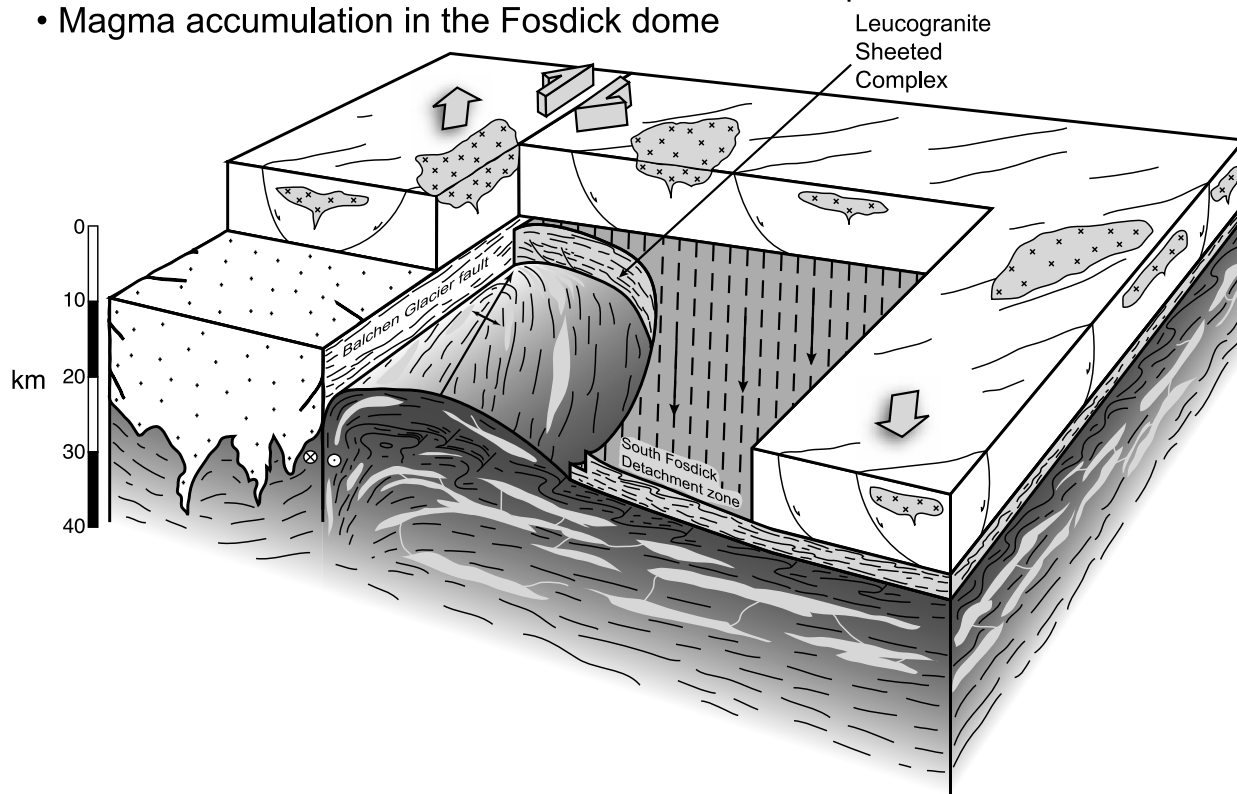


Figure 11. Three-dimensional block diagrams of the Fosdick dome that show the relationship between the divergence angle (α) and fabrics in partially molten crust. (a) Depicts the wrench ($\alpha = 0^\circ$) phase of deformation, displaying the role of the Fosdick dome as a region of melt transfer. (b) Depicts the oblique divergence ($\alpha = 45^\circ$) phase of deformation and shows the Fosdick dome as a magma accumulation zone.

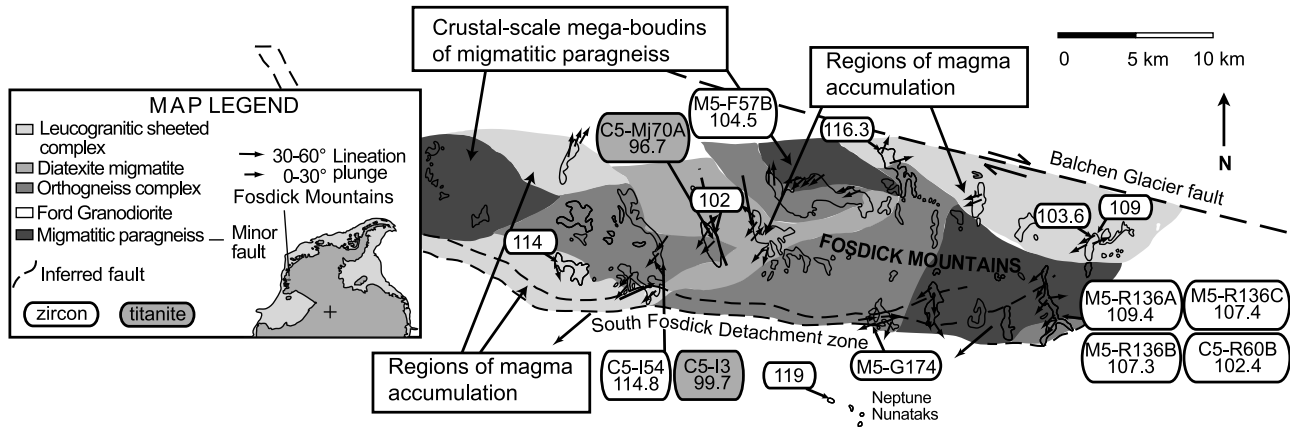


Figure 12. Geologic map pattern interpretation that shows the distribution of structures, regions of magma accumulation (represented by the diatexite migmatite and the leucogranite sheeted complex), and corresponding Cretaceous U-Pb ages. The interpretation shows mega-boudins of migmatitic paragneiss that may have created pressure gradients that influenced melt flow and magma accumulation.

as the trend of the maximum stretching axis of strain. The difference in angle between the stretching axis and the 100° – 280° trend of the Balchen Glacier fault equates with a divergence angle of 45° [McFadden *et al.*, 2010]. For a divergence angle of that magnitude, subhorizontal fabrics and oblique stretching are predicted in a setting of oblique divergence (extension-dominated transtension) [Teyssier and Tikoff, 1999] (Figure 11b). As the angle of divergence increased, one would expect a change in rock fabrics from constrictional to plane strain, and for horizontal foliation to strengthen and vertical shortening to prevail, resulting in the transposition of early steep fabrics and the attraction of linear fabric elements toward the direction of divergence [Passchier, 1997; Teyssier and Tikoff, 1999]. Within the Fosdick dome, in general, transitions from steep foliations to subhorizontal foliations are spatially abrupt. The transition in divergence angle, from low ($0^{\circ} + 10^{\circ}$) to intermediate (45°) was sufficiently rapid to not produce intermediate fabrics, which would be expected to be purely lineated tectonites (L-tectonites). An isolated example of L-tectonites within the South Fosdick Detachment zone at Mount Richardson may preserve a fabric that developed during the presumed foliation switch under constrictional strain; however, this isolated occurrence could also be associated with local strain compatibility.

[54] The steep and shallow patterning of the foliated rocks appears to control the sites of granite emplacement in the middle crust [e.g., Weinberg *et al.*, 2009]. In the paragneisses at Mount Avers and the western Fosdick range, steep foliations and megascopic folds attributed to Devonian–Carboniferous deformation are preserved, largely unaffected by Cretaceous deformation (Figure 5a). The lack of effects of Cretaceous deformation may be due to the refractory, residual character of the paragneisses [Korhonen *et al.*, 2010a] that rendered them mechanically strong and resistant to deformation. Residual paragneisses underwent prior high temperature metamorphism and crustal melting during the Devonian–Carboniferous, when the Ford Granodiorite was emplaced [Siddoway *et al.*, 2004b; Siddoway and

Fanning, 2009; Korhonen *et al.*, 2010a]. We hypothesize that the competent residual paragneiss blocks may have created large-scale strain perturbations that caused pressure gradients to develop, causing melts formed from Cretaceous migmatization to migrate along pressure gradients to the ENE and WSW. The diatexite migmatite unit and the leucogranite sheeted complex represent regions of magma accumulation down gradient from the residual blocks that are interpreted as mega-boudins (Figure 12).

6.2. Timescale for the Evolution of Oblique Motion

[55] SHRIMP U-Pb ages of granite and leucosome that are emplaced in steep versus subhorizontal foliation

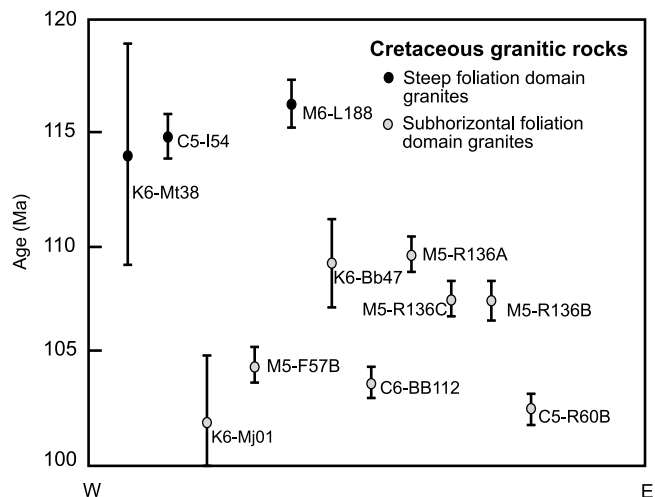


Figure 13. Summary diagram showing SHRIMP U-Pb zircon weighted mean ages versus qualitative geographic position. Black circles represent the older samples that were emplaced in steep structures and gray circles represent the younger samples that were emplaced in subhorizontal foliations or within the South Fosdick Detachment zone.

domains are used to assess the timing and duration of magma crystallization and metamorphic events in the Fossdick Mountains during oblique extensional deformation associated with the West Antarctic Rift system (Figures 8, 9, and 10; Table 1). These data are employed to examine the timing of fabric development and constrain the transition from wrench to oblique divergence (Figure 11). The origin of the granites as crustal melts near their source region is indicated by the low Th/U ratios for the majority of Cretaceous zircon rim analyses (Table 1). Low Th/U ratios may be consistent with a metamorphic origin for the rims [Williams and Claesson, 1987]. Alternatively, the very high U concentrations in these analyses may indicate U enrichment and the low Th/U ratios may be due to zircon growth in an U enriched partial melt [e.g., Schaltegger *et al.*, 1999].

[56] Cretaceous granites and leucosomes from the Fossdick dome consist of two age groups. The older group yields ages between ca. 117 and 114 Ma and a younger group has ages between ca. 109 and 102 Ma [McFadden *et al.*, 2010; Korhonen *et al.*, 2010b] (Figure 13). The older ages come from granites emplaced within steep foliation domains that commonly are recumbently folded with the dominant subhorizontal metamorphic layering. A folded, steeply dipping leucogranite sill (M6-L188) has an age of 116.3 ± 1.0 Ma [McFadden *et al.*, 2010]. The recumbently folded granite sheet (C5-I54) (Figure 6a) and a granite emplaced in a steep foliation (K6-Mt38) have ages of 114.8 ± 1.1 Ma (Figure 8a) and 114 ± 5 Ma, respectively. These samples (C5-I54 and K6-Mt38) both have Sr-Nd isotope compositions, elevated Zr, trace element compositions, and REE patterns that suggest a Ford Granodiorite source [Korhonen *et al.*, 2010b].

[57] The younger granites found within the subhorizontal foliation domains or within the South Fossdick Detachment zone gave ages between ca. 109 and 102 Ma [Korhonen *et al.*, 2010b; McFadden *et al.*, 2010]. The 20 cm-thick subhorizontal granite sill (M5-F57B) that cuts the diatexite migmatite unit at Mount Ferranto has a U-Pb zircon age of 104.5 ± 0.8 Ma (Figure 8b). A subhorizontal leucogranite sheet (C6-BB112) and a subhorizontal granite (K6-Bb47), both from within the leucogranite sheeted complex at Bird Bluff, have U-Pb zircon ages of 103.6 ± 0.7 Ma and 109 ± 2 Ma, respectively. The boudinaged granodioritic orthogneiss (M5-R136A) from within the detachment zone at Mount Richardson has zircon analyses that fall into two age subgroups, one $^{206}\text{Pb}/^{238}\text{U}$ age of 109.1 ± 0.8 Ma and the other $^{206}\text{Pb}/^{238}\text{U}$ age of 105.4 ± 1.0 Ma (Figure 9a). There is no evident difference in morphology, U ppm, Th ppm, or Th/U ratio (Table 1), or REE and trace element concentrations of the zircons grains that yield the two rim ages (Figure 9f; Table 2). A concordant biotite granite (M5-R136C) and a discordant granite-filled shear band (M5-R136B) yield indistinguishable ages of 107.4 ± 0.8 Ma and 107.3 ± 0.9 Ma, respectively (Figures 9b and 9c). Situated within mesoscale extensional structures that record dextral oblique, top-to-the-SW motion within the South Fossdick Detachment zone, the granites are syntectonic with respect to motion in the zone (Figures 6c and 6d). The 100 m-thick

tabular leucogranite sheet (C5-R60B) preserves a magmatic fabric, intruded the gneissic foliation, and it has interdigitated margins with the gneisses. We interpret the concordant granite as a late syntectonic emplacement into the detachment zone (Figure 6e). The age of the tabular leucogranite sheet (C5-R60B) is 102.4 ± 0.7 Ma (Figure 9d).

[58] The difference in emplacement ages for granites in the subhorizontal domains versus granites in the steep domains, presented here and in McFadden *et al.* [2010] may be used to estimate the timeframe for the transition from wrench to oblique extension. The youngest U-Pb age from a granite emplaced in a steep foliation domain is ca. 114 Ma and the oldest U-Pb age from granite emplaced in a subhorizontal foliation domain is ca. 109 Ma. We interpret the ages to mean that the transition from wrench to extension-dominated transtension accommodated on the South Fossdick Detachment zone occurred in as little as 5 Ma.

[59] The late to post-tectonic discordant diorite dikes, C5-I3 and C5-Mj70A, emplaced between ca. 102 and 97 Ma, provide a lower limit on the time of movement upon the South Fossdick Detachment zone and on dome emplacement. The diorite dike from southern Mount Iphigene (C5-I3) is folded within the gneissic foliation and has an age of 101.2 ± 1.2 Ma (Figures 6a and 10a). The diorite dike (C5-Mj70A) from Marujupu Peak crosscuts the gneissic foliation and has an age of 96.7 ± 1.0 Ma (Figures 6b and 10b). Judging from the pristine character of the prismatic, clear, oscillatory-zoned titanite grains, the $^{206}\text{Pb}/^{238}\text{U}$ ages correspond to crystallization of titanite and the diorite host. The differences in U ppm, Th ppm, and Th/U ratio between titanite samples C5-I3 and C5-Mj70A may indicate that the two dikes are different generations or are extracted from different sources (Table 3). These dikes are similar in age to a post-tectonic two-mica granite stock that has a U-Pb monazite age of ca. 100 Ma [Richard *et al.*, 1994]. The emplacement of the mafic dikes coincided with or only narrowly preceded the rapid cooling of the entire dome that is documented by $^{40}\text{Ar}/^{39}\text{Ar}$ cooling ages between ca. 101 and 94 Ma for hornblende, muscovite, biotite, and K-feldspar across the range [Richard *et al.*, 1994]. The time interval for high temperature metamorphism and generation of crustal melts from 114 to 102 Ma in Marie Byrd Land strengthens the evidence for widespread felsic magmatism upon the East Gondwana margin more broadly (Figure 1), in that there is good correspondence with the timing of magmatism in the large Whitsunday province of Australia [Bryan *et al.*, 2000].

6.3. Melt Transport, Magma Accumulation, and Detachment Initiation

[60] The distribution, fabrics, and ages of granite and leucosome emplaced in steep and subhorizontal foliation domains may be employed to investigate the timescales and pathways of the transport of melt and the accumulation of magma in the Fossdick dome. The presence of concordant leucosome and granite within the steep foliation domains formed during the wrench phase of deformation is evidence that the foliation provided a pathway for movement of

crustal melts produced during high temperature metamorphism [McFadden *et al.*, 2010; Korhonen *et al.*, 2010b] (Figure 11a). These earlier granites (ca. 117–114 Ma) have whole rock and trace element compositions that suggest they may be the less evolved equivalents of the regionally exposed Byrd Coast Granite and that both were likely sourced from the Ford Granodiorite [Korhonen *et al.*, 2010b]. Byrd Coast granite from the nearby hanging wall, at Neptune Nunataks, has a LA-ICP-MS zircon age of ca. 119 ± 8 Ma [Korhonen *et al.*, 2010b] (Figure 2). However, the Ford Granodiorite at the level of the Fosdick Mountains is not a fertile source under the conditions (P, T, aH₂O) of Cretaceous metamorphism, so melt that migrated into the Fosdick Mountains probably came from a deeper crustal level [Korhonen *et al.*, 2010a]. Thus, the inferred subvertical inferred melt pathways appear to have been conduits for melt that migrated through the crust to upper crustal plutons, making the Fosdick dome a melt transfer zone during the wrench phase (Figure 11a).

[61] The younger granites comprising the leucogranite sheeted complex and the subhorizontal diatexite migmatite unit range in age from 109 ± 2 Ma to 102.4 ± 0.7 Ma. The granites have an estimated volume >150 km³ and are interpreted as regions of magma accumulation within the dome, formed after the change in the regional strain field to extension-dominated transtension (Figure 11b). We attribute the change from melt transport to magma accumulation in the Fosdick dome to a rotation of the divergence angle from 0° to 45° during the rapid transition from wrench to transtension [McFadden *et al.*, 2010]. The South Fosdick Detachment zone initiated at approximately the same time as emplacement of the leucogranite sheeted complex according to the new U-Pb zircon data suggesting that the shear zone localized upon the site of the complex.

[62] There are contradictory views about the dynamic relationship between magma accumulation and faults and shear zones [e.g., Neves *et al.*, 1996; Brown and Solar, 1998a; Rosenberg, 2004; Weinberg *et al.*, 2004]. The competing hypotheses are that shear zones control ascent of granite magma [Brown and Solar, 1998a; Weinberg *et al.*, 2004] or magma accumulation initiates the development of shear zones [Neves *et al.*, 1996]. In the Fosdick dome, we find evidence that both processes occurred. The transcurrent Balchen Glacier fault system likely focused the ascent and transfer of magma during the wrench phase, leading to an accumulation of voluminous magma that led to initiation of the South Fosdick Detachment zone. The presence of subhorizontal granite sheets along most of the length of the South Fosdick Detachment zone (Figure 2) lends support to our interpretation that magma accumulated prior to the detachment initiation. In this scenario, the addition of volume and heat from granite magma within the leucogranite sheeted complex led to melt-induced weakening and initiation of the detachment [e.g., Teyssier *et al.*, 2005]. The tabular intrusions in the detachment zone that are syntectonic show that melt transfer continued for a short period, however the motion on the detachment concluded by ca. 99–97 Ma, the time of dike emplacement [McFadden *et al.*, 2007]. The rapid cooling of the dome, documented from

⁴⁰Ar/³⁹Ar data [Richard *et al.*, 1994], undoubtedly contributed to the lack of tectonic overprinting and to the wholesale preservation of the structural-magmatic relationships in the dome.

[63] The crosscutting relationships between structures that host granite and leucosome and faults allow us to develop a relative and an absolute chronology that highlights the relationship between oblique extensional deformation and magma emplacement. The Fosdick dome provides extraordinary insight into the spatial and temporal inter-relationships among melt transport, magma accumulation, and detachment initiation and development.

7. Summary

[64] In the Fosdick Mountains, transcurrent deformation affecting heterogeneous crust controlled the development of foliation, the emplacement of leucosome and granite layers concordant to gneissic fabric, and accumulation of a large volume of magma in the leucogranite sheeted complex and the diatexite migmatite unit. Overprinting of steep foliation domains by subhorizontal structures may indicate that the Fosdick dome developed due to a change in the divergence angle from wrench ($\alpha = 0^\circ$) to oblique divergence ($\alpha = 45^\circ$). The timing and duration of the change in kinematics is bracketed by an older group of granites that intruded subvertical foliation, with U-Pb zircon ages between ca. 117 and 114 Ma, and a younger group of granites in subhorizontal sheets with U-Pb zircon ages between ca. 109 and 102 Ma. During wrench tectonics, the Fosdick dome acted as a melt transfer zone for melt and magma transport to higher crustal levels. Polyphase metamorphism imparted heterogeneities in the crust that created strain and pressure gradients that drove melt migration. Thus, when the divergence angle rotated toward extension-dominated transtension (oblique divergence), dilation zones formed and voluminous magmatic sheets accumulated in the Fosdick dome. The granite emplacement ages show that the transition from wrench to oblique divergence occurred in as little as 5 Ma. The correspondence in timing between the change from vertical melt transport to lateral accumulation of granite and the initiation of the detachment indicates that the rotation of the divergence angle was the critical factor in exhumation of the rapidly cooled Fosdick dome.

[65] **Acknowledgments.** This manuscript has been improved by extensive and insightful reviews of an earlier version by R. Weinberg, A. Tulloch, and Associate Editor R. Miller. We thank D. L. Whitney for significant contributions to ideas presented in this work and comments on earlier drafts of this paper. Companion studies by Fawna Korhonen, Tetsu Saito, and Mike Brown aided the formulation of hypotheses presented here. We thank Seth Kruckenberg and Jenny Haywood for fieldwork collaboration; Sylvie Fadrhonc, Chuck Magee, Sam Mertens, and Brenda Armstrong for contributions to the SHRIMP research; and Mike Roberts, Allen O'Bannon, and Forrest McCarthy for field coordination and safety. For logistical support, we thank employees of Raytheon Polar Services (Berg Field Center and USAP Cargo, in particular), ANG 109th, and Kenn Borek Air crews. Research was funded by the National Science Foundation Office of Polar Programs grants NSF-OPP 0338279 to C.S. Siddoway and NSF-OPP 0337488 to C. Teyssier, but the authors are fully responsible for the scientific content.

References

- Adams, C. J. (1986), Geochronological studies of the Swanson Formation of Marie Byrd Land, West Antarctica, and correlation with northern Victoria Land, East Antarctica and the South Island, New Zealand, *N.Z. J. Geol. Geophys.*, **29**, 345–358.
- Adams, C. J. (1987), Geochronology of granite terranes in the Ford Ranges, Marie Byrd Land, West Antarctica, *N.Z. J. Geol. Geophys.*, **30**, 51–72.
- Aleinikoff, J. N., R. P. Wintsch, R. P. Tollo, D. M. Unruh, C. M. Fanning, and M. D. Schmitz (2007), Ages and origins of rocks of the Killingworth dome, south-central Connecticut: Implications for the tectonic evolution of southern New England, *Am. J. Sci.*, **307**, 63–118, doi:10.2475/01.2007.04.
- Bellot, J. P. (2007), Pre- to syn-extensional melt-assisted nucleation and growth of extensional gneiss domes: The western French Massif Central (Variscan belt), *J. Struct. Geol.*, **29**, 863–880, doi:10.1016/j.jsg.2007.01.001.
- Black, L. P., S. L. Kamo, C. M. Allen, J. N. Aleinikoff, D. W. Davis, R. J. Korsch, and C. Foudulis (2003), TEMORA 1: A new zircon standard for Phanerozoic U-Pb geochronology, *Chem. Geol.*, **200**, 155–170, doi:10.1016/S0009-2541(03)00165-7.
- Bradshaw, J. D., B. Andrew, and B. D. Field (1983), Swanson Formation and related rocks of Marie Byrd Land and a comparison with the Robertson Bay Group of Northern Victoria Land, in *Antarctic Earth Science*, edited by R. L. Oliver et al., pp. 274–279, Austr. Acad. of Sci., Canberra.
- Bradshaw, J. D., R. J. Pankhurst, S. D. Weaver, B. C. Storey, R. J. Muir, and T. R. Ireland (1997), New Zealand superterrane recognized in Marie Byrd Land and Thurston Island, in *The Antarctic Region, Geological Evolution and Processes*, edited by C. A. Ricci, pp. 429–436, Terra Antarctica, Siena, Italy.
- Brown, M. (1994), The generation, segregation, ascent and emplacement of granite magma: The migmatite-to-crustally derived granite connection in thickened orogens, *Earth Sci. Rev.*, **36**, 83–130, doi:10.1016/0012-8252(94)90009-4.
- Brown, M. (2007), Crustal melting and melt extraction, ascent and emplacement in orogens: Mechanisms and consequences, *J. Geol. Soc.*, **164**, 709–730, doi:10.1144/0016-76492006-171.
- Brown, M. (2008), Granites, migmatites and residual granulites: Relationships and processes, *Short Course Ser.* **38**, pp. 97–144, Mineral. Assoc. Canada, Quebec City, Quebec, Canada.
- Brown, M., and G. S. Solar (1998a), Shear zone systems and melts: Feedback relations and self-organisation in orogenic belts, *J. Struct. Geol.*, **20**, 211–227, doi:10.1016/S0191-8141(97)00068-0.
- Brown, M., and G. S. Solar (1998b), Granite ascent and emplacement during contractional deformation in convergent orogens, *J. Struct. Geol.*, **20**, 1365–1393, doi:10.1016/S0191-8141(98)00074-1.
- Bryan, S. E., A. Ewart, C. J. Stephens, J. Parianos, and P. J. Downes (2000), The Whitsunday Volcanic Province, central Queensland, Australia: Lithological and stratigraphic investigations of a silicic-dominated large igneous province, *J. Volcanol. Geotherm. Res.*, **99**, 55–78, doi:10.1016/S0377-0273(00)00157-8.
- Collins, W. J., and E. W. Sawyer (1996), Pervasive granulitoid magma transfer through the lower-middle crust during non-coaxial compressional deformation, *J. Metamorph. Geol.*, **14**, 565–579, doi:10.1046/j.1525-1314.1996.00442.x.
- D'Lemos, R. S., M. Brown, and R. A. Strachan (1992), Granite magma generation, ascent and emplacement within a transpressional orogen, *J. Geol. Soc.*, **149**, 487–490, doi:10.1144/gsjgs.149.4.0487.
- Davey, F. J., and G. Brancolini (1995), The late Mesozoic and Cenozoic structural setting of the Ross Sea region, in *Geology and Seismic Stratigraphy of the Antarctic Margin*, *Antarct. Res. Ser.*, vol. 68, edited by A. K. Cooper, P. F. Barker, and G. Brancolini, pp. 167–182, AGU, Washington, D. C.
- Ferraccioli, F., E. Bozzo, and D. Damaske (2002), Aeromagnetic signatures over western Marie Byrd Land provide insight into magmatic arc basement, mafic magmatism and structure of the eastern Ross Sea rift flank, *Tectonophysics*, **347**, 139–165, doi:10.1016/S0040-1951(01)00242-6.
- Fitzgerald, P. G., and S. L. Baldwin (1997), Detachment fault model for the evolution of the Ross Embayment, in *The Antarctic Region: Geological Evolution and Processes*, edited by C. A. Ricci, pp. 555–564, Terra Antarctica, Siena, Italy.
- Flowers, R. M., S. A. Bowring, A. J. Tulloch, and K. A. Klepeis (2005), Temperature of burial and exhumation within the deep roots of a magmatic arc, Fiordland, New Zealand, *Geology*, **33**, 17–20, doi:10.1130/G211010.1.
- Forster, M. A., and G. S. Lister (2003), Cretaceous metamorphic core complexes in the Otago Schist, New Zealand, *Aust. J. Earth Sci.*, **50**, 181–198, doi:10.1046/j.1440-0952.2003.00986.x.
- Fossen, H., and B. Tikoff (1993), The deformation matrix for simultaneous simple shearing, pure shearing and volume change, and its application to transpression–transension tectonics, *J. Struct. Geol.*, **15**, 413–422, doi:10.1016/0191-8141(93)90137-Y.
- Foster, D. A., P. T. Doughty, T. J. Kalakay, C. M. Fanning, S. Coyner, W. C. Grice, and J. Vogl (2007), Kinematics and timing of exhumation of metamorphic core complexes along the Lewis and Clark fault zone, northern Rocky Mountains, USA, in *Exhumation Associated With Continental Strike-Slip Fault Systems*, edited by A. B. Till et al., *Spec. Pap. Geol. Soc. Am.*, **434**, 207–232, doi:10.1130/2207.2434(10).
- Gibson, G. M., I. McDougall, and T. R. Ireland (1988), Age constraints on metamorphism and the development of a metamorphic core complex in Fiordland, southern New Zealand, *Geology*, **16**, 405–408, doi:10.1130/0091-7613(1988)016<0405:ACOMAT>2.3.CO;2.
- Guo, J., S. Y. O'Reilly, and W. L. Griffin (1996), Zircon inclusions in corundum megacrysts: I. Trace element geochemistry and clues to the origin of corundum megacrysts in alkali basalts, *Geochim. Cosmochim. Acta*, **60**, 2347–2363, doi:10.1016/0016-7037(96)00084-1.
- Hasalová, P., K. Schulmann, O. Lexa, P. Stipska, F. Hrouda, S. Ulrich, J. Haloda, and P. Tycova (2008), Origin of migmatites by deformation-enhanced melt infiltration of orthogneiss: A new model based on quantitative microstructural analysis, *J. Metamorph. Geol.*, **26**, 29–53.
- Hollis, J. A., G. L. Clarke, K. A. Klepeis, N. R. Daczko, and T. R. Ireland (2004), The regional significance of Cretaceous magmatism and metamorphism in Fiordland, New Zealand, from U-Pb zircon geochronology, *J. Metamorph. Geol.*, **22**, 607–627, doi:10.1111/j.1525-1314.2004.00537.x.
- Hoskin, P. W. O. (1998), Minor and trace element analysis of natural zircon (ZrSiO₄) by SIMS and laser ablation ICP-MS: A consideration and comparison of two broadly competitive techniques, *J. Trace Microprobe Tech.*, **16**, 301–326.
- Hoskin, P. W. O., and U. Schaltegger (2003), The composition of zircon and igneous and metamorphic petrogenesis, *Rev. Mineral. Geochem.*, **53**, 27–62, doi:10.2113/0530027.
- Hutton, D. H. W. (1988), Granite emplacement mechanisms and tectonic controls: Inferences from deformation studies, *Trans. R. Soc. Edinburgh Earth Sci.*, **79**, 245–255.
- Ireland, T. R., and G. M. Gibson (1998), SHRIMP monazite and zircon geochronology of high-grade metamorphism in New Zealand, *J. Metamorph. Geol.*, **16**, 149–167, doi:10.1111/j.1525-1314.1998.00112.x.
- Ireland, T. R., and F. Wlotzka (1992), The oldest zircons in the solar system, *Earth Planet. Sci. Lett.*, **109**, 1–10, doi:10.1016/0012-821X(92)90069-8.
- Ireland, T. R., T. Flottmann, C. M. Fanning, G. M. Gibson, and W. V. Preiss (1998), Development of the early Paleozoic Pacific margin of Gondwana from detrital-zircon ages across the Delamerian orogen, *Geology*, **26**, 243–246, doi:10.1130/0091-7613(1998)026<0243:DOTEPP>2.3.CO;2.
- Kimbrough, D. L., and A. J. Tulloch (1989), Early Cretaceous age of orthogneiss from the Charleston Metamorphic Group, New Zealand, *Earth Planet. Sci. Lett.*, **95**, 130–140, doi:10.1016/0012-821X(89)90172-6.
- Korhonen, F. J., M. Brown, S. Saito, and C. Siddoway (2010a), Modeling multiple melt loss events in the evolution of an active continental margin, *Lithos*, **116**, 230–248, doi:10.1016/j.lithos.2009.09.004.
- Korhonen, F. J., S. Saito, M. Brown, C. S. Siddoway, and J. M. D. Day (2010b), Multiple generations of granite in the Fostick Mountains, Marie Byrd Land, West Antarctica: Implications for polyphase intra-crustal differentiation in a continental margin setting, *J. Petrol.*, **51**, 627–670, doi:10.1093/petrology/egg093.
- Kula, J., A. J. Tulloch, T. L. Spell, and M. L. Wells (2007), Two-stage rifting of Zealandia–Australia–Antarctica: Evidence from ⁴⁰Ar/³⁹Ar thermochronometry of the Sisters shear zone, Stewart Island, New Zealand, *Geology*, **35**, 411–414, doi:10.1130/G23432A.1.
- Ludwig, K. R. (2001), SQUID 1.02: A user's manual, *Spec. Publ. 2*, Berkeley Geochron. Cent., Berkeley, Calif.
- Ludwig, K. R. (2003), User's manual for Isoplot/Ex, version 3.0: A geochronological toolkit for Microsoft Excel, *Spec. Publ. 4*, Berkeley Geochron. Cent., Berkeley, Calif.
- Luyendyk, B. (1995), Hypothesis for Cretaceous rifting of East Gondwana caused by subducted slab capture, *Geology*, **23**, 373–376, doi:10.1130/0091-7613(1995)023<0373:HFCROE>2.3.CO;2.
- Luyendyk, B. P., D. S. Wilson, and C. S. Siddoway (2003), Eastern margin of the Ross Sea Rift in western Marie Byrd Land: Crustal structure and tectonic development, *Geochim. Geophys. Geosyst.*, **4**(10), 1090, doi:10.1029/2002GC000462.
- Maas, R., P. D. Kinny, I. S. Williams, D. O. Froude, and W. Compston (1992), The Earth's oldest known crust: A geochronological and geochemical study of 3900–4200 Ma old detrital zircons from Narryer and Jack Hills, Western Australia, *Geochim. Cosmochim. Acta*, **56**, 1281–1300, doi:10.1016/0016-7037(92)90062-N.
- Marchildon, N., and M. Brown (2003), Spatial distribution of melt-bearing structures in anatectic rocks from southern Brittany: Implications for melt-transfer at grain-to orogen-scale, *Tectonophysics*, **364**, 215–235, doi:10.1016/S0040-1951(03)00061-1.
- McFadden, R., C. S. Siddoway, C. Teyssier, C. M. Fanning, and S. C. Kruckenberg (2007), Cretaceous oblique detachment tectonics in the Fostick Mountains, Marie Byrd Land, Antarctica, in *Antarctica: A Keystone in a Changing World - Online Proceedings of the 10th ISAES*, edited by A. K. Cooper et al., *U.S. Geol. Surv. Open File Rep.* 2007–1047, 6 pp., doi:10.3133/of2007-1047.srp046.
- McFadden, R. R., C. Teyssier, C. S. Siddoway, D. L. Whitney, and C. M. Fanning (2010), Oblique dilation, melt transfer, and gneiss dome emplacement, *Geology*, **38**, 375–378, doi:10.1130/G30493.1.
- Milord, L., E. W. Sawyer, and M. Brown (2001), Formation of diatexite migmatite and granite magma during anatexis of semi-pelitic metasedimentary rocks: An example from St. Malo, France, *J. Petrol.*, **42**, 487–505, doi:10.1093/petrology/42.3.487.
- Mortimer, N., A. J. Tulloch, R. N. Spark, N. W. Walker, E. Ladley, A. Allibone, and D. L. Kimbrough

- (1999), Overview of the Median Batholith, New Zealand: A new interpretation of the geology of the Median Tectonic Zone and adjacent rocks, *J. Afr. Earth Sci.*, 29, 257–268, doi:10.1016/S0899-5362(99)00095-0.
- Mortimer, N., K. Hoernle, F. Hauff, J. M. Palin, W. J. Dunlap, R. Werner, and K. Faure (2006), New constraints on the age and evolution of the Wishbone Ridge, southwest Pacific Cretaceous microplates, and Zealandia–West Antarctica breakup, *Geology*, 34, 185–188, doi:10.1130/G22168.1.
- Muir, R., T. R. Ireland, S. D. Weaver, and J. D. Bradshaw (1994), Ion microprobe U–Pb zircon geochronology of granitic magmatism in the western province of the South Island, New Zealand, *Chem. Geol.*, 113, 171–189, doi:10.1016/0009-2541(94)90011-6.
- Muir, R. J., T. R. Ireland, S. D. Weaver, J. D. Bradshaw, T. E. Waight, R. Jongens, and G. N. Eby (1997), SHRIMP U–Pb geochronology of Cretaceous magmatism in northwest Nelson–Westland, South Island, New Zealand, *N.Z. J. Geol. Geophys.*, 40, 453–463.
- Muir, R., T. R. Ireland, S. D. Weaver, J. D. Bradshaw, J. A. Evans, G. N. Eby, and D. Shelley (1998), Geochronology and geochemistry of a Mesozoic magmatic arc system, Fiordland, New Zealand, *J. Geol. Soc.*, 155, 1037–1053, doi:10.1144/gsjgs.155.6.1037.
- Mukasa, S. B., and I. W. D. Dalziel (2000), Marie Byrd Land, West Antarctica: Evolution of Gondwana's Pacific margin constrained by zircon U–Pb geochronology and feldspar common-Pb isotopic compositions, *Geol. Soc. Am. Bull.*, 112, 611–627, doi:10.1130/0016-7606(2000)112<611:MBLWAE>2.0.CO;2.
- Neves, S. P., A. Vauchez, and C. J. Archanjo (1996), Shear zone-controlled magma emplacement or magma-assisted nucleation of shear zone? Insights from northeast Brazil, *Tectonophysics*, 262, 349–364, doi:10.1016/0040-1951(96)00007-8.
- Oldow, J. S. (2003), Active transtensional boundary zone between the western Great Basin and Sierra Nevada block, western U.S. Cordillera, *Geology*, 31, 1033–1036, doi:10.1130/G19838.1.
- Olsen, S. N., B. D. Marsh, and L. P. Baumgartner (2004), Modelling mid-crustal migmatite terrains as feeder zones for granite plutons: The competing dynamics of melt transfer by bulk versus porous flow, *Trans. R. Soc. Edinburgh Earth Sci.*, 95, 49–58, doi:10.1017/S0263593300000912.
- Pankhurst, R. J., S. D. Weaver, J. D. Bradshaw, B. C. Storey, and T. R. Ireland (1998), Geochronology and geochemistry of pre-Jurassic superterranes in Marie Byrd Land, Antarctica, *J. Geophys. Res.*, 103, 2529–2547, doi:10.1029/97JB02605.
- Passchier, C. W. (1997), The fabric attractor, *J. Struct. Geol.*, 19, 113–127, doi:10.1016/S0191-8141(96)00077-6.
- Richard, S. M. (1992), Structure and cooling history of the Fosdick Metamorphic Complex, Marie Byrd Land, West Antarctica, in *Recent Progress in Antarctic Earth Science*, edited by Y. Yoshida et al., pp. 289–294, Terra, Tokyo.
- Richard, S. M., C. H. Smith, D. L. Kimbrough, P. G. Fitzgerald, B. P. Luyendyk, and M. O. McWilliams (1994), Cooling history of the northern Ford Ranges, Marie Byrd Land, West Antarctica, *Tectonics*, 13, 837–857, doi:10.1029/93TC03322.
- Rosenberg, C. L. (2004), Shear zones and magma ascent: A model based on a review of the Tertiary magmatism in the Alps, *Tectonics*, 23, TC3002, doi:10.1029/2003TC001526.
- Sambridge, M. S., and W. Compston (1994), Mixture modeling of multicomponent data sets with application to ion-probe zircon ages, *Earth Planet. Sci. Lett.*, 128, 373–390, doi:10.1016/0012-821X(94)90157-0.
- Sawyer, E. W. (1996), Melt segregation and magma flow in migmatites: Implications for the generation of granite magmas, *Trans. R. Soc. Edinburgh Earth Sci.*, 87, 85–94.
- Sawyer, E. W. (2001), Melt segregation in the continental crust: Distribution and movement of melt in anatectic rocks, *J. Metamorph. Geol.*, 19, 291–309, doi:10.1046/j.0263-4929.2000.00312.x.
- Sawyer, E. W. (2008), Working with migmatites: Nomenclature for the constituent parts, *Short Course Ser.*, 38, pp. 1–28, Mineral. Assoc. Canada, Quebec City, Quebec, Canada.
- Schaltegger, U., C. M. Fanning, D. Günther, J. C. Maurin, K. Schulmann, and D. Gebauer (1999), Growth, annealing and recrystallization of zircon and preservation of monazite in high-grade metamorphism: Conventional and in-situ U–Pb isotope, cathodoluminescence and microchemical evidence, *Contrib. Mineral. Petrol.*, 134, 186–201, doi:10.1007/s004100050478.
- Scott, J. M., and A. F. Cooper (2006), Early Cretaceous extensional exhumation of the lower crust of a magmatic arc: Evidence from the Mount Irene Shear Zone, Fiordland, New Zealand, *Tectonics*, 25, TC3018, doi:10.1029/2005TC001890.
- Siddoway, C. S. (2008), Tectonics of the West Antarctic rift system: New light on the history and dynamics of distributed intracontinental extension, in *Antarctica: A Keystone in a Changing World*, edited by A. K. Cooper et al., pp. 91–114, Natl. Acad. of Sci., Washington, D. C.
- Siddoway, C. S., and C. M. Fanning (2009), Paleozoic tectonism on the East Gondwana margin: Evidence from SHRIMP U–Pb zircon geochronology of a migmatite-granite complex in West Antarctica, *Tectonophysics*, 262–277, doi:10.1016/j.tecto.2009.04.021.
- Siddoway, C. S., S. L. Baldwin, P. G. Fitzgerald, C. M. Fanning, and B. P. Luyendyk (2004a), Ross Sea mylonites and the timing of intracontinental extension within the West Antarctic rift system, *Geology*, 32, 57–60, doi:10.1130/G20005.1.
- Siddoway, C. S., S. M. Richard, C. M. Fanning, and B. P. Luyendyk (2004b), Origin and emplacement of a middle Cretaceous gneiss dome, Fosdick Mountains, West Antarctica, in *Gneiss Domes in Orogeny*, edited by D. L. Whitney et al., *Spec. Pap. Geol. Soc. Am.*, 380, 267–294.
- Siddoway, C. S., L. C. Sass III, and R. Esser (2005), Kinematic history of Marie Byrd Land terrane, West Antarctica: Direct evidence from Cretaceous mafic dykes, in *Terrane Processes at the Margin of Gondwana*, edited by A. Vaughan et al., *Geol. Soc. Spec. Publ.*, 246, 417–438.
- Siddoway, C. S., R. McFadden, C. Teyssier, C. M. Fanning, and R. Vail (2008), Characterization of melt-transfer to accumulation in a transcurrent shear zone using U–Pb SHRIMP geochronology, meso- and microstructures of granites, Fosdick Mountains, Antarctica, *Geol. Assoc. Can. Mineral. Assoc. Can. Abstr.*, 33, 158–159.
- Smith, C. H. (1997), Mid-crustal processes during Cretaceous rifting, Fosdick Mountains, Marie Byrd Land, in *The Antarctic Region: Processes and Evolution*, edited by C. A. Ricci et al., pp. 313–320, Terra Antarctica, Siena, Italy.
- Solar, G. S., and M. Brown (2001), Deformation partitioning during transpression in response to Early Devonian oblique convergence, northern Appalachian orogen, USA, *J. Struct. Geol.*, 23, 1043–1065, doi:10.1016/S0191-8141(00)00175-9.
- Storey, B., T. Leat, S. D. Weaver, R. J. Pankhurst, J. D. Bradshaw, and S. Kelley (1999), Mantle plumes and Antarctica–New Zealand rifting: Evidence from mid-Cretaceous mafic dykes, *J. Geol. Soc.*, 156, 659–671, doi:10.1144/gsjgs.156.4.0659.
- Talbot, J.-V., M. Faure, Y. Chen, and G. Martelet (2005), Pull-apart emplacement of the Margeride granitic complex (French Massif Central): Implications for the late evolution of the Variscan orogen, *J. Struct. Geol.*, 27, 1610–1629, doi:10.1016/j.jsg.2005.05.008.
- Tera, F., and G. Wasserberg (1972), U–Th–Pb systematics in three Apollo 14 basalts and the problem of initial Pb in lunar rocks, *Earth Planet. Sci. Lett.*, 14, 281–304, doi:10.1016/0012-821X(72)90128-8.
- Teyssier, C., and B. Tikoff (1999), Fabric stability in oblique convergence and divergence, *J. Struct. Geol.*, 21, 969–974, doi:10.1016/S0191-8141(99)00067-X.
- Teyssier, C., and D. L. Whitney (2002), Gneiss domes and orogeny, *Geology*, 30, 1139–1142, doi:10.1130/0091-7613(2002)030<1139:GDAO>2.0.CO;2.
- Teyssier, C., E. C. Ferre, D. L. Whitney, B. Norlander, O. Vanderhaeghe, and D. Parkinson (2005), Flow of partially molten crust and origin of detachments during collapse of the Cordilleran Orogen, in *High-Strain Zones: Structures and Physical Properties*, *Geol. Soc. Spec. Publ.*, 245, 39–64, doi:10.1144/GSL.SP.2005.245.01.03.
- Tikoff, B., and C. Teyssier (1992), Crustal-scale, en echelon “P-shear” tensional bridges: A possible solution to the batholithic room problem, *Geology*, 20, 927–930, doi:10.1130/0091-7613(1992)020<0927:CSEEPS>2.3.CO;2.
- Tikoff, B., and C. Teyssier (1994), Strain modeling of displacement-field partitioning in transpressional orogens, *J. Struct. Geol.*, 16, 1575–1588, doi:10.1016/0191-8141(94)90034-5.
- Tulloch, A. J., and D. L. Kimbrough (1989), The Paparoa metamorphic core complex, New Zealand: Cretaceous extension associated with fragmentation of the Pacific margin of Gondwana, *Tectonics*, 8, 1217–1234, doi:10.1029/TC008i006p01217.
- Tulloch, A. J., and D. L. Kimbrough (2003), Paired plutonic belts in convergent margins and the development of high Na, Al, Sr, low Y magmatism: The Peninsular Ranges Batholith of California and the Median Batholith of New Zealand, in *Tectonic Evolution of the Northwestern Mexico and the Southwestern USA*, edited by S. E. Johnson et al., *Spec. Publ. Geol. Soc. Am.*, 374, 275–295.
- Tulloch, A. J., M. Beggs, J. Kula, T. Spell, and N. Mortimer (2006), Cordillera Zealandia, the Sisters Shear Zone and their influence on the early development of the Great South Basin, paper presented at New Zealand Petroleum Conference, Wellington. (Available at www.crownminerals.govt.nz/cms/petroleum/conferences/conference-proceedings-2006.)
- Tulloch, A. J., J. Ramezani, D. L. Kimbrough, K. Faure, and A. H. Allibone (2009), U–Pb geochronology of Paleozoic plutonism in western New Zealand: Implications of S-type granite generation and growth of the east Gondwana margin, *Geol. Soc. Am. Bull.*, 121, 1236–1261, doi:10.1130/B26272.1.
- Vanderhaeghe, O. (2001), Melt segregation, pervasive melt migration and magma mobility in the continental crust: The structural record from pores to orogens, *Phys. Chem. Earth, Part A*, 26, 213–223.
- Vernon, R. H., G. L. Clarke, and W. J. Collins (1990), Local, mid-crustal granulite facies metamorphism and melting: An example in the Mount Stafford area, central Australia, in *High Temperature Metamorphism and Crustal Anatexis*, edited by J. R. Ashworth and M. Brown, pp. 272–319, Unwin-Hyman, London.
- Wade, F. A., C. A. Cathey, and J. B. Oldham (1978), Reconnaissance geologic map of the Gutenko Nunataks quadrangle, Marie Byrd Land, Antarctica, USARP Antarctic Geological Map A-11, scale 1:250,000, U. S. Geol. Surv. Reston, Va.
- Weaver, S. D., J. D. Bradshaw, and C. J. Adams (1991), Granitoids of the Ford Ranges, Marie Byrd Land, Antarctica, in *Geological Evolution of Antarctica*, edited by M. R. A. Thomson et al., pp. 345–351, Cambridge Univ. Press, Cambridge, U. K.
- Weaver, S. D., C. J. Adams, R. J. Pankhurst, and I. L. Gibson (1992), Granites of Edward VII Peninsula, Marie Byrd Land: Anorogenic magmatism related to Antarctic–New Zealand rifting, in *Proceedings of the Second Hutton Symposium on the Origin of Granites and Related Rocks*, edited by E. Brown and B. W. Chappell, pp. 281–290, R. Soc. of Edinburgh, Edinburgh, U. K.
- Weaver, S. D., B. C. Storey, R. J. Pankhurst, S. B. Mukasa, V. Divenere, and J. D. Bradshaw (1994), Antarctic–New Zealand rifting and Marie Byrd Land lithospheric magmatism linked to ridge subduction and mantle plume activity, *Geology*, 22,

- 811–814, doi:10.1130/0091-7613(1994)022<0811:ANZRAM>2.3.CO;2.
- Weinberg, R. F., and G. Mark (2008), Magma migration, folding and disaggregation of migmatites in the Karakoram shear zone, Ladakh, NW India, *Geol. Soc. Am. Bull.*, 120, 994–1009, doi:10.1130/B26227.1.
- Weinberg, R. F., A. N. Sial, and G. Mariano (2004), Plutons and shear zones in the Borborema Province, Brazil, *Geology*, 32, 377–380, doi:10.1130/G20290.1.
- Weinberg, R. F., G. Mark, and H. Reichardt (2009), Magma ponding in the Karakoram shear zone, Ladakh, NW India, *Geol. Soc. Am. Bull.*, 121, 278–285.
- Whitney, D. L., C. Teyssier, and M. T. Heizler (2007), Gneiss domes, metamorphic core complexes, and wrench zones: Thermal and structural evolution of Nigde Massif, central Anatolia, *Tectonics*, 26, TC5002, doi:10.1029/2006TC002040.
- Williams, I. S. (1998), U-Th-Pb geochronology by ion microprobe, in *Applications of Microanalytical Techniques to Understanding Mineralizing Processes*, *Rev. Econ. Geol.*, edited by M. A. McKibben et al., vol. 7, pp. 1–35, Soc. of Econ. Geol., Littleton, Colo.
- Williams, I. S., and S. Claesson (1987), Isotopic evidence for the Precambrian provenance and Caledonian metamorphism of high grade paragneisses from the Seve Nappes, Scandinavian Caledonides: II. Ion microprobe zircon U–Th–Pb, *Contrib. Mineral. Petrol.*, 97, 205–217, doi:10.1007/BF00371240.
- C. M. Fanning, Research School Earth Sciences, Australian National University, Canberra, ACT 0200, Australia.
- R. R. McFadden, Smithsonian Tropical Research Institute, Apartado 0843-03092, Balboa, Ancon, Panama.
- C. S. Siddoway, Department of Geology, Colorado College, Colorado Springs, CO 80903, USA.
- C. Teyssier, Department of Geology and Geophysics, University of Minnesota, Minneapolis, MN 55455, USA.